

Towards Practical Autonomous Flight Simulation for Flapping Wing Biomimetic Robots with Experimental Validation

Chen Qian, Yongchun Fang, *Senior Member, IEEE*, Fan jia, Jifu Yan, Yiming Liang and Tiefeng Li

Abstract—Tried-and-true flapping wing robot simulation is essential in developing flapping wing mechanisms and algorithms. This paper presents a novel application-oriented flapping wing platform, highly compatible with various mechanical designs and adaptable to different robotic tasks. First, the blade element theory and the quasi-steady model are put forward to compute the flapping wing aerodynamics based on wing kinematics. Translational lift, translational drag, rotational lift, and added mass force are all considered in the computation. Then we use the proposed simulation platform to investigate the passive wing rotation and the wing-tail interaction phenomena of a particular flapping-wing robot. With the help of the simulation tool and a novel statistic based on dynamic differences from the averaged system, several behaviors display their essence by investigating the flapping wing robot dynamic characteristics. After that, the attitude tracking control problem and the positional trajectory tracking problem are both overcome by robust control techniques. Further comparison simulations reveal that the proposed control algorithms compared with other existing ones show apparent superiority. What is more, with the same control algorithm and parameters tuned in simulation, we conduct real flight experiments on a self-made flapping wing robot, and obtain similar results from the proposed simulation platform. In contrast to existing simulation tools, the proposed one is compatible with most existing flapping wing robots, and can inherently drill into each subtle behavior in corresponding applications by observing aerodynamic forces and torques on each blade element.

Index Terms—Biologically-inspired robots, biomimetics, dynamics, flapping wing.

I. INTRODUCTION

SIMULATING flapping wing flight within practical robotic tasks can help analyze and build flapping wing robots, as well as various associated algorithms. On the other hand, possibly only through application-oriented environmental interactions, sufficiently precise modelings, platforms allowing nuanced observations, we can decipher flapping flight to a

novel stage. Furthermore, if a simulation platform can stimulate the development of different flapping wing robots, it should be sufficiently compatible and expandable to different robot designs.

Compared with state-of-art conventional unmanned aerial vehicle studies, flapping wing robot researches remain in a relatively elementary stage. Researchers aspire to bridge the gap between aerodynamics studies, mechanism studies, and robotic studies [1–7]. In [2], Karásek *et al.* develop an X-shape wings tailless robot with servos rotating the flapping mechanism and asynchronous bilateral flapping wing actuation, which can imitate the rapid escape maneuvers of flies. Tu *et al.* design a hummingbird-inspired, at-scale, tail-less flapping wing micro aerial vehicle, which independently controls its wings with a total of only two directly driven motors [3]. Zufferey *et al.* develop an Eagle-inspired Flapping-wing robot E-Flap that can carry a 100% of the payload, which has two aero-elastic wings [5]. Chen *et al.* design a novel bat-style flapping wing robot, which couples or decouples the morphing and flapping, and can generate a bilateral asymmetric downstroke affording high rolling agility [6]. These prototypes possess considerable disparities. Flapping wing robots and algorithms developments strongly depend on experimental studies and empirical knowledge concluded from data-rich conventional planes or drones, meanwhile, flapping wing aerodynamic investigations and specific robotic task studies are virtually disengaged.

Flapping wing flight simulation can provide profound inspiration and instructions for real flight tasks. In [8], Fei *et al.* provide an open-source high fidelity dynamic simulation for their flapping wing robot. After applying system identification, the same flight performance can be achieved on the robot by directly implementing the controller in simulation. However, the aerodynamics computation of wings is highly simplified, which hinders the observation of each blade element aerodynamics in simulation, and unable to simulate subtle aerodynamic behaviors such as center of pressure (CoP) 2D positional changing on the wing surface. Furthermore, the tailless design of their robot makes the attendant simulation rarely consider wing-tail or wing-wing aerodynamic interaction. This hinders its application for many other flapping wing robots with tails or tandem wings. Although their simulation can be integrated into the Robot Operating System (ROS) and Gazebo, many applications involving environment building, perception, and interaction tasks remain elusive and obviously require cumbersome additional programming. Thus, substan-

This work was supported by National Natural Science Foundation of China under Grant 62233011, T2125009, 92048302. (Corresponding authors: Yongchun Fang and Tiefeng Li.)

C. Qian and Y. Liang are with Interdisciplinary Innovation Research Centers, Intelligent Robotic Research Center, Zhejiang Laboratory, Hangzhou 311100, China (e-mail: qianc@zhejianglab.com, liangym@zhejianglab.com).

Y. Fang, F. Jia, J. Yan, are with College of Artificial Intelligence, Nankai University, and Institute of Robotics and Automatic Information Systems, Nankai University, Tianjin, 300353, China (e-mail: fangyc@nankai.edu.cn, fanjia@mail.nankai.edu.cn).

T. Li is with School of Aeronautics and Astronautics, ZheJiang University, Hangzhou 310012, China (e-mail: litiefeng@zju.edu.cn).

tial improvement of this simulation platform is indispensable and imperative. In [9], Orłowski *et al.* use a system of three rigid bodies including the body and two wings to simulate the flapping wing robot, and further conclude that mass effects of the wings can exert non-negligible influence on dynamics, stability, and control analyses. However, there still exists no wing-tail or wing-wing interaction. Moreover, the absence of an interface limits its easy-to-use potential for robotic applications. In [10], Lopez-Lopez *et al.* propose a simple but effective analytical model for a specific flapping wings UAV in longitudinal gliding flight, and the corresponding environment has been built on Unreal Engine 4 for rendering. The simulation switches between aerodynamic model and collision model for their different dynamics, and supports both flapping and gliding flights. Regretfully, the wing aerodynamics is also possibly over-simplified, such that delicate observation is not optional. And the bespoke mode makes the simulation limited in extensibility. In [11], He *et al.* establish a simulation model for flapping wing robot longitudinal motion. Nevertheless, the simulation is dedicated to the control task, and due to the longitudinal limitation, it is difficult to implement for most flapping wing robot tasks.

In conclusion, the practical flapping wing flight simulation platform should have the following characteristics:

- 1) The simulation platform should consider both the distinctive modeling aerodynamics and the multi-body dynamics. The wing-wing and wing-tail aerodynamics interactions should also be investigated.
- 2) The platform can be compatible with different modeling configurations. And different designs can be losslessly transformed into its simulation counterpart.
- 3) In the simulation, different robotic tasks can be performed. Furthermore, the platform ideally provides a user-friendly interface for widely used robotic software or algorithms that can be smoothly integrated into online programs for real flight.

The main purpose of this paper is to realize the simulation platform and validate it with experiments. Quasi-steady aerodynamics model and blade element method are the common recipes for modeling flapping-wings. Quasi-steady models are usually used to describe the unsteady process with basic principles and empirical formulae, which provide a tractable means of calculating instantaneous forces from defined or generated wing kinematics [12]. When using blade element theory, aerodynamic forces computations are performed on spanwisely divided wing strips, which naturally considers wing aerodynamics spatial heterogeneity. Due to the computation simplicity, relatively high fidelity and high compatibility to control dynamic models, many works involving flapping wing aerodynamics implement these methods [13–16]. Most simulation platforms are first tested with control tasks, meanwhile, the control problem is also the main distinctive part of flapping wing robotic tasks [8–11, 17–19]. Thus, we use attitude tracking and trajectory tracking tasks to test the proposed simulation platform, meanwhile, other conventional robotic tasks such as perception and navigation can also be straightforwardly performed.

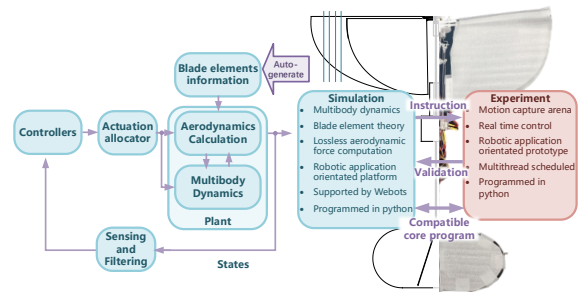


Fig. 1. Flapping wing robot simulation platform and experiment.

This work develops an open-source simulation platform satisfying the aforementioned three characteristics. The contributions can be concluded into the following four aspects:

- 1) Most existing flapping wing robots can be realized on the developed simulation platform without any complicated adaptation, which can help design, modify and validate both the robot itself and the algorithm thereon. By bridging the gap between algorithms designed for an individual robots in a bespoke fashion, the proposed platform can accelerate the flapping wing design and test process.
- 2) In contrast to existing simulations, aerodynamic force computations in the proposed simulation are losslessly implemented, allowing us to investigate a variety of subtle behaviors in robotic tasks. The simulation fidelity is sufficiently high that both algorithms and parameters can be directly applied in real flight even without identification. This can help us understand unexpected behaviors owing to complicated flapping wing aerodynamics, which can also be utilized to explore natural flight behaviors.
- 3) A highly extensible real flight program framework is developed. The real flight algorithm shares the same algorithms and parameters in simulation, which facilitates applying the optimal algorithms and parameters obtained from simulation results.
- 4) A novel and theoretically more effective statistic capturing the flapping wing oscillating dynamics is proposed.

The remainder of this paper is organized as follows. Section II explains the basic aerodynamics used in the simulation. Section III studies the specific flapping wing robot aerodynamics performance, where a self-made X-shape tailed flapping wing robot is used as an example. In Section IV, practical robotic applications are performed. We respectively study the attitude tracking and positional trajectory tracking problem for the robot, and compare them with other existing controllers to show their superiority. Then in Section V, the real counterpart robot is built, and the real flight program framework is developed. The real flight experiments are performed to validate the simulation results. Finally, Section VI concludes this work.

II. FLAPPING WING AERODYNAMICS

A. Quasi-steady Aerodynamics

The unsteady aerodynamics force mechanisms in flapping flight such as leading-edge vortex, added mass, wake capture, rotational circulation, and clap-and-fling effect should be well

considered in order to obtain an accurate aerodynamic or dynamic model. Conducting a large amount of simulations require an easily computed model. The combination of the blade element theory and the quasi-steady models can actually strike a satisfactory balance between simplicity and fidelity, which depends on the instantaneous wing kinematics such as velocities and accelerations, as well as the wing morphology. From another perspective, they are modeled by the assumption of inherently time-independent fluid dynamic mechanisms [20–22]. Specifically, the local force acting on a wing strip, or blade element, can be integrated over the wingspan to obtain the aerodynamic forces acting on the wings. The wake capture mechanism is excluded in our simulation for the following two reasons: its inherent dependence on the airflow history, and its insignificant contribution to improving flying efficiency [23]. Generally, the instantaneous aerodynamics force can be calculated in the following manner:

$$\mathbf{F} = \mathbf{F}_{t,\text{lift}} + \mathbf{F}_{t,\text{drag}} + \mathbf{F}_r + \mathbf{F}_a \quad (1)$$

where $\mathbf{F}_{t,\text{lift}}$ is the translational lift, acting perpendicular to the wing velocity, $\mathbf{F}_{t,\text{drag}}$ is the translational drag, opposing the wing velocity, \mathbf{F}_r is rotational force caused by the rotational circulation, associated with the wing pronation or supination, and \mathbf{F}_a is the added mass force, which is associated with the wing acceleration. Based on the quasi-steady model given in [21], the aforementioned forces interact synergistically, but for conciseness can be calculated as

$$\begin{aligned} \text{Mag}(\mathbf{F}_{t,\text{lift}}) &= \sum \frac{1}{2} \rho c \|\mathbf{u}_w\|^2 C_{Lt}(\alpha) \Delta r, \\ \text{Mag}(\mathbf{F}_{t,\text{drag}}) &= \sum \frac{1}{2} \rho c \|\mathbf{u}_w\|^2 C_{Dt}(\alpha) \Delta r, \\ \text{Mag}(\mathbf{F}_r) &= \sum \rho c^2 \|\dot{\alpha}\| \|\mathbf{u}_w\| C_r \Delta r, \\ \text{Mag}(\mathbf{F}_a) &= \sum \frac{\rho \pi c^2}{4} \left\{ \frac{\mathbf{u}_w \cdot \dot{\mathbf{u}}_w}{\|\mathbf{u}_w\|} \sin \alpha + \|\dot{\mathbf{u}}_w\| \alpha \cos \alpha \right\} \Delta r \end{aligned} \quad (2)$$

where $\text{Mag}(\star)$ indicates the magnitude of the corresponding force, which can be positive or negative depended on the angle of attack (AoA) α , ρ is the air density, c is the chord length, \mathbf{u}_w is the wing-strip (*i.e.* the blade element) effective velocity, Δr is the wing-strip width, $C_{Lt}(\alpha)$ and $C_{Dt}(\alpha)$ are the translational lift and drag coefficients, respectively, C_r is the rotational coefficient, and α is the effective AoA, which is calculated by incorporating with the resultant rotation from the torso to the wing chord. Each blade element may have a different AoA due to the temporally and spatially varying flow, such that the local orientations of lift and drag also differ.

Based on the experiments reported in [24], besides the free-stream velocity, the flapping wing induced velocity also obviously affects the tail aerodynamic forces. Since the flapping wing induced wake is complex and fast with respect to the tail movement, we can use the actuator disk model to estimate the average flapping wing induced velocity instead. This average velocity \mathbf{u}_i is considered in the opposite direction to the resultant force of the translational lifts generated by wings:

$$\mathbf{u}_i = \frac{1}{2} \frac{\Sigma \mathbf{F}_{t,\text{lift}}}{\|\Sigma \mathbf{F}_{t,\text{lift}}\|} \sqrt{\frac{\|\Sigma \mathbf{F}_{t,\text{lift}}\|}{S_d} \frac{1}{2\rho}} \quad (3)$$

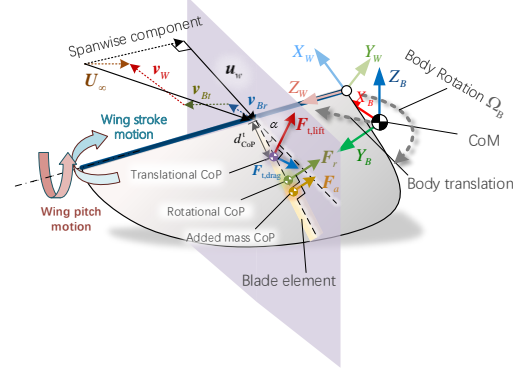


Fig. 2. The schematic of the flapping wing aerodynamics, where CoP means the center of pressure, and CoM means the center of mass.

where $\Sigma \mathbf{F}_{t,\text{lift}}$ is the resultant force of translational lifts, and S_d is the actuator disk area.

B. Blade Elements

The concept of blade element is to separate the wing spanwisely into several wing strips. In order to determine the chord length of each strip, we provide a method to automatically extract them from 3D-model files¹. We first get the vertices points cloud of the wing, then use a linear interpolation algorithm to obtain a functional description of the wing edge. Subsequently, we use the polynomial function to help generate an appropriate quantity of aequilate blade elements.

First, we demonstrate our way to formulate the wing strip effective incident flow velocity \mathbf{u}_w . Although there are several other impact factors such as the induced downwash flow [22], the jet induced by the shed vortices [25], *etc.*, in order to make the model more easily computed, we follow the assumption that any span-wise component of the relative velocity has no effect on the wing forces [26], and neglect the downwash flow and the vortex shedding, hence we can concentrate on the body motion induced velocity (both translational \mathbf{v}_{Bt} and rotational \mathbf{v}_{Br}), the free flow \mathbf{U}_∞ , and the wing motion induced velocity \mathbf{v}_W . The effective velocity \mathbf{u}_w is then given by

$$\begin{aligned} \mathbf{u}_w &= \mathbf{u}_{\omega r} - \hat{\mathbf{n}}_S (\hat{\mathbf{n}}_S \cdot \mathbf{u}_{\omega r}), \\ \mathbf{u}_{\omega r} &\triangleq \mathbf{U}_\infty - \mathbf{v}_W - \mathbf{v}_{Bt} - \mathbf{v}_{Br} \end{aligned} \quad (4)$$

where $\hat{\mathbf{n}}_S$ is the normal vector of the plane that contains the chord, and is also perpendicular to the wing rotation axis.

The relationship between these velocities is shown in Fig.2. And the effective AoA α is the angle between the chord and the effective incident velocity, which is shown as

$$\alpha = \arccos \frac{\mathbf{u}_w \cdot \hat{\mathbf{c}}}{\|\mathbf{u}_w\| \|\hat{\mathbf{c}}\|} \quad (5)$$

where $\hat{\mathbf{c}}$ is the vector along the chord direction. Note that all the velocities are resolved at the leading edge even if the force act on the wing strip CoP, to accentuate that flapping

¹See source codes at <https://github.com/Chainplain/BladeEleBuilder>.

translation refers to an airfoil revolving around a central axis [22]. And based on [20], we can specify the relationship between the coefficients and the AoA:

$$C_{Lt} = A_L \sin(2\alpha), \quad (6)$$

$$C_{Dt} = C_{D_0} + A_D [1 - \cos(2\alpha)] \quad (7)$$

where the coefficients C_{Lt} and C_{Dt} are both functions of Reynolds number Re :

$$A_L = 1.966 - 3.94Re^{-0.429},$$

$$A_D = 1.873 - 3.14Re^{-0.369},$$

$$C_{D_0} = 0.031 + 10.48Re^{-0.764}.$$

As suggested in [27] and also reported in [12], by using the theoretical value of the standard Kutta–Joukowski theory, the rotation coefficient can be given as

$$C_r = \pi (0.75 - \hat{x}_0) \quad (8)$$

where \hat{x}_0 is the non-dimensional rotational axis chordwise position, the value of which ranges from 0 to 1.

Second, we consider the aerodynamic moment, which is extremely important for wing passive rotation, and highly sensitive to changes in the location of the CoP. The moment can be shown similarly to the semi-empirical formulae given in (2). However, to pursue consistency and conciseness, we use the deduction given in [27], which points out that the CoP due to rotational force is located at 1/2 non-dimensional chord position. And we further use the model proposed in [28] to obtain the CoP due to translational force:

$$\hat{d}_{CoP}^t = \frac{1}{\pi} |\alpha|, \quad 0 \leq \alpha \leq \frac{\pi}{2} \quad (9)$$

Furthermore, since the leading edge and the pitch rotational axis of the FWAV coincide with each other in this work, also according to [28], the CoP due to added mass is located at 9/16 non-dimensional chord position. Since the clap-and-fling mechanism depends on wings contact, the induced aerodynamic moments can be neglected because their effect is canceled by each other. Once CoPs are determined, we can find the specific lengths of force arms, and corresponding aerodynamic moments can then be straightforwardly computed.

To facilitate the simulation in the sense of conciseness, we need the following assumption.

Assumption 1 (Torsional spring): Similar to [32], we assume that there exist torsional springs at hinges in pitch rotations, which provides a simplification of the wing flutter and flexibility.

With respect to the tail aerodynamics, we follow the same model as the wings. The only difference is, in the tail aerodynamics, the flapping wing induced velocity u_i is considered, such that we use the resultant velocity of free flow velocity U_∞ and induced velocity u_i to calculate the wing effective incident velocity, instead of only the free flow velocity. The tandem flapping wings can also be simulated in a similar way.

III. AERODYNAMICS SIMULATION PERFORMANCE

In order to demonstrate the correctness and accuracy of our simulation, also to manifest its sophistication degree,

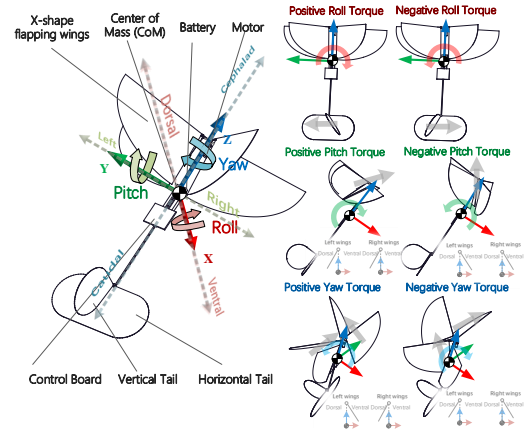


Fig. 3. Schematic of the flapping wing robot used in this section simulation: three-dimensional body fixed frame consists of three orthogonal axes, where the X-axis is red, Y-axis green, Z-axis blue, and the gray arrow indicates the average lift direction of corresponding wings or tails.

we provide close shots of wing passive rotation and wing-tail interaction phenomena, which are well-known intractable aerodynamic behaviors in flapping wing simulations. Furthermore, we also show that the proposed simulation tool can help compute periodically average forces and torques, which can penetrate the maneuverability characteristics of the robot. The robot simulated in this section with its body-fixed frame is shown in Fig. 3. It is an X-wing flapping wing robot, whose equilibrium pitch position is adjustable, with a fixed horizontal tail and a revolute vertical tail. The robot can generate roll torques by rotating its vertical tail. When left wings and right wings equilibrium pitch position is moved along the same direction, the robot can generate pitch torques. When left wings and right wings equilibrium pitch position is moved along opposite directions, the robot generates yaw torques. Detailed robot parameters are collectively given in TABLE I.

A. Passive Wing Rotation

Although the torsional spring assumption, *Assumption 1*, is relatively simple, due to the detailed aerodynamics simulation, the locomotions and effects are comparatively complex. In most flapping wing robots, powered by motors, and driven by crank-and-rod mechanism, the flapping wing stroke angle are sinusoidal or approximately sinusoidal in time. Thus, we suppose the stroke angle is also sinusoidal in our simulation. In all the simulations, the stroke peak to peak amplitude is set as $\pi/4$ rad for each wing, the air density is set as 1.29 kg/m^3 , the simulation step is 1 ms. We also install a stopper at the pitch rotation joint, which can limit the rotation angle within the range of $[-\pi/4, \pi/4]$ rad, because at the aerodynamic AoA of $\pi/4$ rad, flapping wing is believed to be most efficient. In the following, we explain those complex flapping wing behaviors by studying different cases. And according to the characteristics of the flapping wing model used in the simulation, the average Reynolds number Re is 7000. The wing with 14 cm spanwise length is divided into 40 blade element strips, meanwhile, the vertical and the horizontal

TABLE I
FLAPPING WINGS SIMULATION PARAMETERS

Parameters	Values	Parameters	Values
mass, m	22g	wing stop pitch angle	$\pi/4$
Reynolds number, Re	7000	pitch balance	$[-\frac{\pi}{4}, \frac{\pi}{4}]$
wing span	30cm	position range	$[-\frac{\pi}{4}, \frac{\pi}{4}]$
air density, ρ	1.29kg/m ³	rudder rotation range	$[-\frac{\pi}{4}, \frac{\pi}{4}]$
wing torsional spring constant	0.025N · m/rad	simulation gap	1 ms
		controller	
		computation gap	10 ms

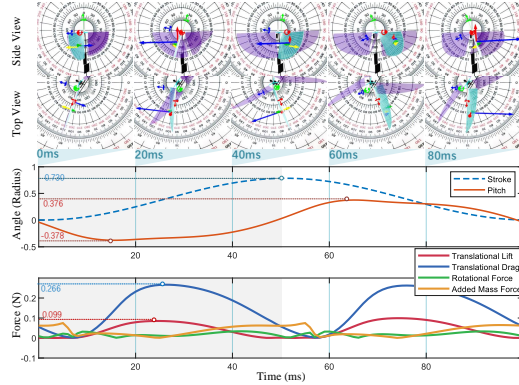


Fig. 4. Flapping wing simulation results when the torsional spring constant is set as 0.025 N · m/rad, stroke frequency at 10 Hz. The curves record the states of the flapping wing marked in light blue. Please note that only the aerodynamics of the upper left wing is displayed to avoid confusion.

tails are both divided into 20 blade element strips, and other number of strips is also optional.

1) *Low-frequency stroke*: we obtain the simulation result shown in Fig. 4. The 3D views in the first two rows can provide a direct demonstration of the wing locomotion in a single period of flapping. Due to the passive rotation mechanism, the pitch angle has a delay of approximately half period. Since the stroke frequency is relatively low, the pitch angle is smaller than the most efficient $\pi/4$ rad. Because of this, the translation drag amplitude shown in the figure is obviously larger than the one of the translational lift. Moreover, we can also see a symmetry between the back-stroke (dark-background part) and the front-stroke (light-background part). The added mass force becomes obvious, with a maximum magnitude of 0.08 N, when the wing starts to accelerate or decelerate. And the rotational force peaks when the wing rotates rapidly. However, there is a rotational force trough instead of a peak when the stroke direction changes, it owes to the drop of the efficient velocity u_w . After the transient ascent, the rotational force descends again, as the pitch rotation subsides. All these behaviors conform to existing works of flapping wing aerodynamics studies, which manifests the accuracy of our simulation.

2) *High frequency stroke*: When we set the torsional spring constant as 0.025 N · m/rad, and stroke frequency as 15 Hz, we obtain the simulation result shown in Fig. 5. Comparing to the results shown in Fig. 4, the aerodynamic forces are relatively large because of the larger AoA, although they demonstrate the similar periodic pattern. As the pitch angle reaches the desired $\pi/4$, the translation lift versus translational

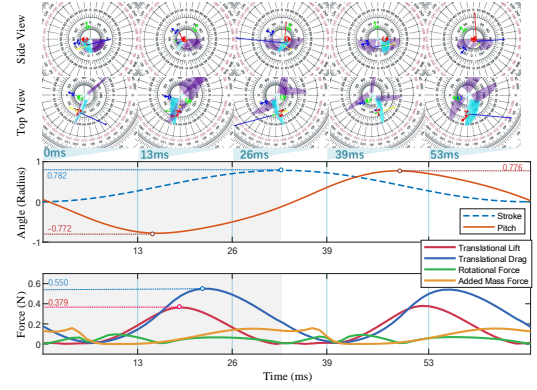


Fig. 5. Flapping wing simulation results when the torsional spring constant is set as 0.025 N · m/rad, stroke frequency at 15 Hz. The curves record states of the flapping wing marked in light blue.

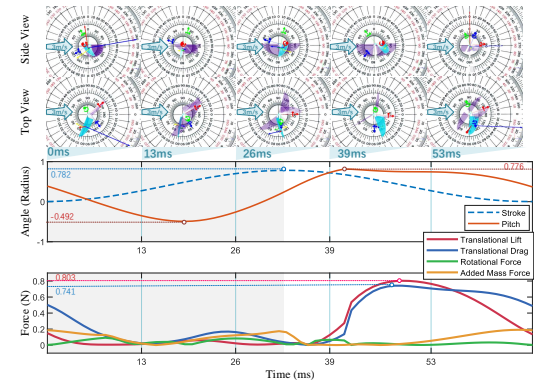


Fig. 6. Flapping wing simulation results when the torsional spring constant is set as 0.025 N · m/rad, stroke frequency at 15 Hz, and the flapping wings faces the 3 m/s wind towards the inertia frame z -direction. The curves record states of the flapping wing marked in light blue.

drag ratio increases. Moreover, both the rotational force and the added mass force periodic patterns are kept similar to those in *Case 1*.

3) *Side wind*: When we set the torsional spring constant as 0.025 N · m/rad, and stroke frequency as 15 Hz, we obtain the simulation result shown in Fig. 6. Moreover, we additionally exert a wind of 3 m/s in the inertia frame z -direction. The magnitudes of aerodynamic forces decrease to comparatively small values, when the wing approximately moves along the wind direction. Clearly shown in Fig. 6, the maximum pitch angle is 0.776 rad, while the minimum is -0.492 rad, which manifests the wing passive locomotion asymmetry. On the other hand, in the front stroke, where the wings move against the wind, these forces magnitudes are larger than they appear in no wind situations shown in *Case 2*. Furthermore, the pitch angle keeps the stop angle $\pi/4$ rad for a relatively long time, such that the high lift-drag ratio is also kept for over 25% period. In conclusion, the side wind causes an asymmetry between front and back stroke. Especially, due to the asymmetry in translational drag, the corresponding effects cannot be periodically averaged into almost zero, which can provide ventral-dorsal forces and body pitch torques.

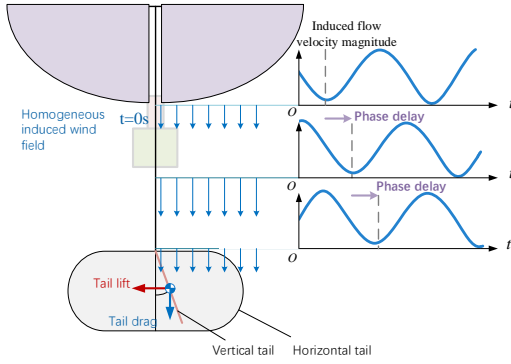


Fig. 7. Schematic of the homogeneous flapping wing induced wind field and its phase delay. The dissipations of these induced velocities are neglected since the traveling distance from the trailing edge to the tail is relatively small.

B. Wing-Tail Interaction

According to our simulation based on the formula (3), as well as PIV test reported in [29], the flapping wing induced velocity has a comparable magnitude as the free-stream velocity does. With respect to our flapping wing robot, and in usual robotic applications, the maximum magnitude of the induced velocity is 2-4 m/s, and the average distance between the flapping edge and the tail is approximately 15 cm, which indicates that the wake traveling delay is about 30-80 ms. Compared with the 50-150 ms flapping wing period length, there is no obvious time scale separation, which induces that the phase delay between the flapping wing aerodynamics and the tail aerodynamics is non-negligible. And based on experimental results provided in [29], there is no prominent spanwise phase delay or magnitude difference, if the distance between the wing trailing edge and the tail is not extremely small. To this end, we use the integrated resultant lift to compute the induced velocity and suppose the wind field is homogeneous within the range of the actuator disk, instead of computing the induced velocity in each individual blade element and floundering in complex wind fields. In this simulation, the induced wind field moves synchronously and caudally within the periodic average speed, where the period is determined by the current flapping wing frequency, which is demonstrated in Fig. 7. Consequently, the current induced velocity actuated on the tail can be obtained by tracing back previous computed flapping wing induced velocity at a specific time point, in order to simulate the phase delay. The reason that we do not set a constant phase delay is the variation of the flapping wing frequency. However, we cannot record indefinitely, such that we set a record truncation with its capacity of 1000 ms record length. If the delay is too large, meaning that the induced velocity is considerably small, then its effect on the rudder can be neglected. Following the above settings, we can simulate the frequency-varying wing-tail interactions, even with changing flapping frequencies and in different free flows.

1) *Periodic tail aerodynamic forces:* The aerodynamic forces of the vertical tail with only the flapping wing induced flow as its incident flow are periodic. In the following simulation case, we only show the changing forces situations when they are periodically stable, which takes several stroke cycles

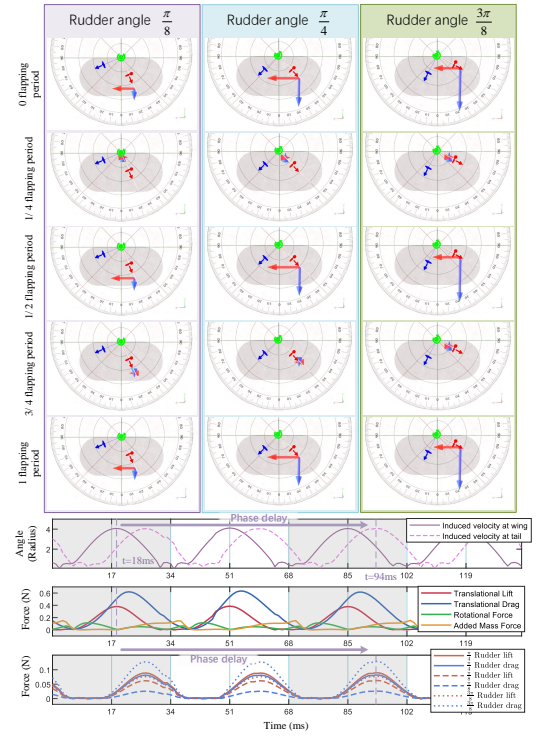


Fig. 8. Periodic aerodynamic forces actuated on the vertical tail with different vertical tail rudder rotation angles. The frame shown is fixed to the vertical tail, whose green axis coincides with the vertical tail rotation axis. The torsional spring constant is set as 0.025 N · m/rad, stroke frequency at 15 Hz, and the rudder rotation angle is set as $\pi/8$, $\pi/4$, and $3\pi/8$, respectively.

after the wings start to flap. As shown in the Fig. 8, due to the symmetry of front and back stroke motion, the aerodynamic forces actuated on the vertical tail changes twice the frequency of the stroke. Similar to the wing aerodynamics, the tail lift reaches its peak when its rotation angle is $\pi/4$, which can also be seen as the aerodynamic AoA in this case. The oscillating forces due to the flapping wing induced incident indicate that, in low speed flight, or hovering flight, the torques generated by the tail are relatively unstable, however, can still achieve efficient maneuver. When the torsional spring constant is set as 0.025 N · m/rad, stroke frequency at 15 Hz, the induced velocity time delay between the wing trailing edge and tail is approximately 76 ms, or approximately 2.269 π long phase delay. The phase delay Φ_d is computed by

$$\Phi_d = 2\pi \frac{T_d}{T_{fp}} \quad (10)$$

where T_d is the time delay, and T_{fp} is the flapping period, equaling to the induced velocity period.

2) *Induced velocity delay:* Furthermore, the relationship between flapping frequencies and delays is analyzed. In this series of simulations, the flapping wing frequency is tested from 5 Hz to 19 Hz with 1 Hz interval, which is the frequently used frequency in most applications of the simulated robot. Based on the simulation result in Fig. 9 (a), the induced velocity time delay descends, as the testing flapping frequency increases, while the decreasing rate decreases. For example, from 5 Hz to 6 Hz, there is a 204 ms induced velocity time

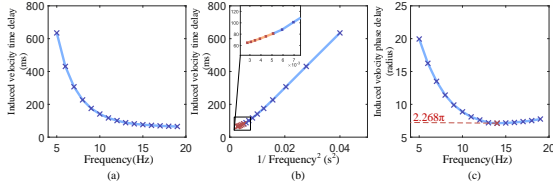


Fig. 9. Flapping wing induced wake traveling time delay and phase delay from wing trailing edge to tail.

TABLE II
FLAPPING WINGS ACTUATION ALLOCATIONS

Fig. show	Pitch Com.	Yaw Com.	Left Wings	Right Wings
10-(a)	$\pi/8$	$-\pi/8$	Dorsal $\pi/4$	Neutral
10-(b)	$\pi/8$	0	Dorsal $\pi/8$	Dorsal $\pi/8$
10-(c)	$\pi/8$	$\pi/8$	Neutral	Dorsal $\pi/4$
10-(d)	0	$-\pi/8$	Dorsal $\pi/8$	Ventral $\pi/8$
10-(e)	0	0	Neutral	Neutral
10-(f)	0	$\pi/8$	Ventral $\pi/8$	Dorsal $\pi/8$
10-(g)	$-\pi/8$	$-\pi/8$	Neutral	Ventral $\pi/4$
10-(h)	$-\pi/8$	0	Ventral $\pi/8$	Ventral $\pi/8$
10-(i)	$-\pi/8$	$\pi/8$	Ventral $\pi/4$	Neutral

delay drop, meanwhile, from 18 Hz to 19 Hz, the drop is only 1 ms. This indicates that, with respect to the simulated robot, the induced flow has its upper limit, albeit the flapping wing frequency can still increase. As shown in Fig. 9 (b), there is a strong proportional relationship between induced velocity time delay and the reciprocal of frequency square, although when the frequency is larger than 14 Hz, this proportional relationship gradually attenuates. Because the coherence between the flapping wing forces and tail generated torques can provide a relatively periodically stable pattern, which cannot be completely captured by the averaged dynamics model, the phase delay is more important in determining the overall robot dynamics and locomotions. The phase delay versus flapping frequency is given in Fig. 9 (c). Based on our observation, there is no obvious strong relationship between flapping wing frequency or its variants. The phase delay sharply decreases from 5 Hz to 10 Hz, then the decrease slows down, and reaches its nadir 2.268π at 14 Hz, and then slowly increases.

C. Aerodynamic Forces and Torques Statistics

Averaging method can capture basic flapping wing robot aerodynamics in relatively stable flight. In the meantime, from a macro perspective of body dynamics, the fluctuations or oscillations components can be neglected to a considerable extent. To facilitate practical robot application, forces and torques macro effects are analyzed within the overall robot, instead of individual wing or deflection surfaces.

1) *Flapping wing dynamics effects*: Averaging method can be applied to flapping wing robot relatively stable flight. Investigating average forces and torques induced by different flapping wings actuation settings can provide fundamental knowledge for robot actuation manner. Furthermore, the oscillation inputs can significantly change the robot overall behaviors, such that we have to investigate and quantify

them. To this end, we propose a statistic based on dynamic differences from the nominal averaged system:

$$v = \sqrt{\sup_{\substack{\tau_1, \tau_2 \in [t_0, t_1] \\ \tau_1 < \tau_2}} \left\| \sum_{s=\tau_1}^{\tau_2} (f(s) - \bar{f}) \cdot l \right\|} \quad (11)$$

for a continuous sampling interval from t_0 to t_1 , where $\sqrt{\star} : \mathbb{R} \rightarrow \mathbb{R}$ is the square root function, $\bar{f} = 1/(t_1 - t_0) \cdot \sum_{s=t_0}^{t_1} f(s)$, l is the simulation step, and f can be selected from the flapping wing forces or torques, which provides a unified oscillation description for flapping wing dynamics under different flapping frequency based on the effects of momentum inputs. The development of this statistic is elaborated in Appendix A. It is noteworthy that only the relative magnitude of v shows practical significance. And since the moment of inertia is not considered in v , this statistic describes the effects of the time-varying force or torque, rather than its consequent kinematic behavior.

When we set the wing pitch torsional spring constant as $0.025 \text{ N} \cdot \text{m/rad}$, and stroke frequency as 5-19 Hz with 2 Hz interval, and also fix the robot with no translational or angular velocity, we obtain the simulation result shown in Fig. 10. The detailed map between torque command and wings pitch balance position settings, is given in TABLE II. Due to the intrinsic unsteadiness and oscillation in flapping wing motions, the force and torques corresponding to the commands, such as pitch command or yaw command, are highly nonlinear and coupled. We list the following four notable phenomena of wing deviated from expectation:

- **PW-1: (Torque-generating inducing thrust drop)** Comparing obtained results in Fig. 10-b,d,f,h with that in Fig. 10-e, respectively, we can find that, when the robot tries to generate pitch or yaw torque with $\pi/8$ wings balance positions changing, there emerges an approximate 23% drop of the thrust.
- **PW-2: (Intrinsic pitch forward)** Simulation tests corresponding to Fig. 10-a,b,c,d,f,g,h,i, when the flapping wing frequency increases, the generated pitch and yaw torques first increase simultaneously, however, start to decrease after 17 Hz, which is highly nonlinear. Meanwhile, the pitch torque increases approximately proportionally to flapping wing frequency, even without a pitch command, because the center of the stroke plane is dorsally displaced from the mass center.
- **PW-3: (Wings asymmetry generating roll torque)** Investigating the test group Fig. 10-a,d,g, and the group Fig. 10-c,f,i, we can find that, when the rotation magnitude of left and right wings pitch balance position is different, the unexpected roll torques arise, which manifests the high coupling characteristic.
- **PW-4: (Saturated oscillation)** The oscillation input slowly increases as the flapping wing frequency increases. However, when the frequency passes 15 Hz, the oscillation input magnitude almost remains stagnant thereafter.

2) *Tail deflection effects*: The aforementioned analyses can also be applied to the tail. The vertical tail rotation method is given in TABLE III. In this simulation, we focus on the flapping wings induced incident velocity acting on

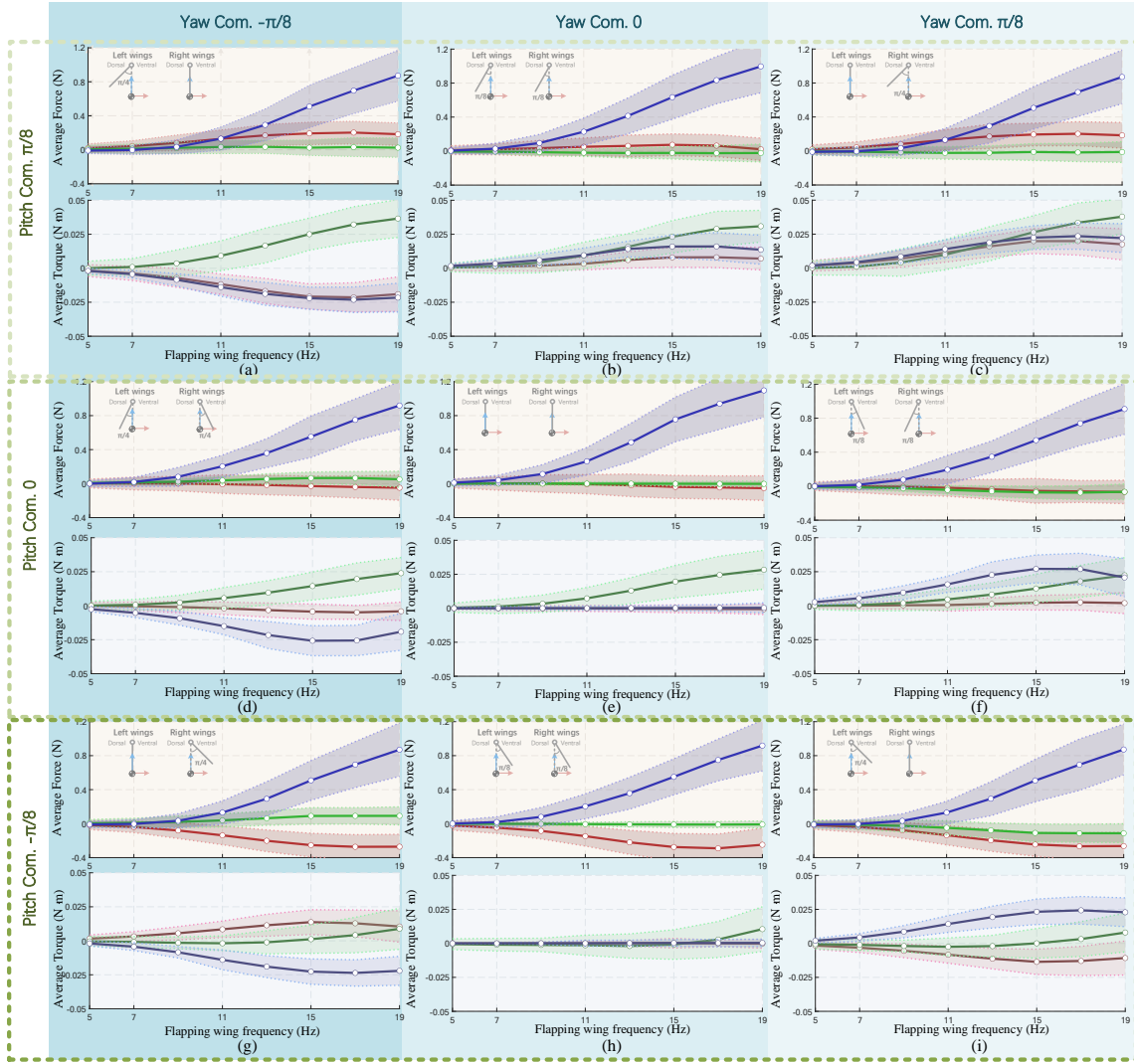


Fig. 10. Resultant average forces and torques by flapping wings with different actuation settings. The left and right wings equilibrium pitch positions are adjusted to generate different torques. Detail wings configurations are sketched at the top left corner in each sub-figure. The forces and torques are all resolved in the body-fixed frame, right-handed system. Forces and torques along X-axis (ventral) are shown as red curves, Y-axis (left) green, Z-axis (cephalad) blue. The shaded area width represents the oscillations that the periodic forces and torques exerted on the robot, v in (11), which is discussed in Appendix A.

TABLE III
VERTICAL TAIL RUDDER ACTUATION ALLOCATIONS

Fig. show	Roll Com.	Rudder
11-1	$-3\pi/8$	Left $3\pi/8$
11-2	$-\pi/4$	Left $\pi/4$
11-3	$-\pi/8$	Left $\pi/8$
11-4	0	Neutral
11-5	$\pi/8$	Right $\pi/8$
11-6	$\pi/4$	Right $\pi/4$
11-7	$3\pi/8$	Right $3\pi/8$

the vertical tail, such that the generated forces and torque are also periodic. Based on our observation of the obtained result shown in Fig. 11, the following two phenomena are noteworthy:

- PR-1: (*Roll peaking at $\pi/4$*) The maximum roll torque appears at the $\pi/4$ rudder rotation. Compared to the torque generated by the wings, when the rudder completely

depends on the flapping wings induced incident flow, the roll torque generated by the rudder introduces more oscillations into the system. Further, we can conclude that there is a strong proportional relationship between flapping wing frequency between 9-17 Hz.

- PR-2: (*Rudder rotation generating Y-axis and Z-axis force*) The coupling between forces and torques is prominent. The rudder induced roll torque substantially depends on the force along Y-axis of the body fixed frame, reflected in the similar patterns shown in Fig. 11, which is due to the salient discrepancy between Y-axis and Z-axis force arms lengths. Furthermore, the deflection of the rudder surface can lead to a maximally 7-10% drop in the robot thrust force.

3) *Velocity induced effects*: From the obtained results shown in Fig. 12, we can investigate the free flow induced dynamics of the robot. In this series of simulations, we set the robot with 0 pitch and 0 yaw commands, and rudder in neutral

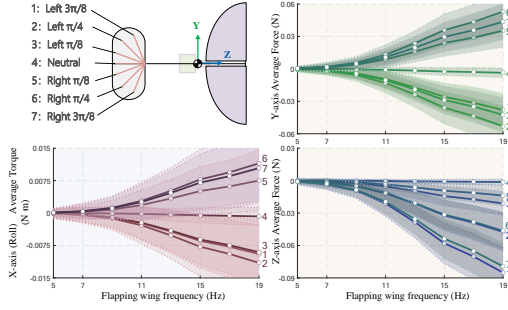


Fig. 11. Forces and torques induced from different vertical tail rudder rotation angles when the flapping wing torsional spring constant is set as $0.025 \text{ N} \cdot \text{m}/\text{rad}$, wing torque command as 0 pitch and 0 yaw. The shaded area width represents the oscillations that the periodic forces and torques exerted on the robot. The vertical tail rudder rotation angle is adjusted to generate different roll torques. The specific rotations are shown in the left upper corner. Forces and torques along X-axis (ventral) are shown as red curves, Y-axis (left) green, Z-axis (cephalad) blue.

position. First, the windless condition shown in Fig. 10-e can be seen as a static reference, where the tail generates no forces or torques such that the robot dynamics completely depends on the wings. Based on our observation of the obtained simulation result shown in Fig. 12, the following three phenomena of free flow induced aerodynamics can be concluded:

- PF-1: (*Resistance force proportional to windward area*) Comparing the pairs (a), (b), and (c) in Fig. 12, we find that there is obvious resistance force in the opposite direction of free flow velocity, whose magnitude is approximately proportional to windward area.
- PF-2: (*Velocity induced pitch*) In the pairs of simulation (a1) and (a2) in Fig. 12, there exists an obvious correlation between Y-axis (pitch) torque and the free flow velocity along the X-axis. The free flow velocity in the negative X-axis direction can induce a negative pitch torque, and vice versa. This phenomenon is similar to the *Pendulum-like dynamics* reported in [24].
- PF-3: (*Velocity induced roll*) In the pairs of simulation (b1) and (b2) in Fig. 12, there also exists an obvious correlation between Z-axis (yaw) torque and the free flow velocity along the Y-axis. The free flow velocity in the negative Y-axis direction can induce a positive pitch torque, and vice versa. This phenomenon is similar to the *Wind-vane-like dynamics* reported in [24].

IV. SIMULATING PRACTICAL ROBOT APPLICATIONS

In the purpose of elaborating that the proposed simulation platform is indeed a flexible, easy-to-use, and application-oriented simulation platform, we demonstrate several robotic applications in this section. In the following simulations, all the above aerodynamic force computations are losslessly implemented, such that we can drill into each subtle behavior in corresponding applications. Simulations are realized on the Webots [30] platform, and programmed mainly in Python.

A. Filtering Oscillations from Flapping Wings

Before entering into the controllers development section, we first need an attitude filter to reduce the oscillations induced

by flapping wings. Previous methods focus on providing smooth feedback signals and sensor fusion[31, 32]. Because the attitude itself is integrated from angular velocity and not excessively oscillating, such that we can straightforwardly use raw attitude data. However, the angular velocity needs filtering to reduce the large-scale oscillation, where a low-pass second order filter is implemented in each channel. The corresponding transfer function is given by

$$H(s) = \frac{\omega_n^2}{s^2 + 2\zeta\omega_n s + \omega_n^2} \quad (12)$$

where $\omega_n \in \mathbb{R}$ is the natural frequency, satisfying $\omega_n = 2\pi f_n$, and $\zeta \in \mathbb{R}$ is the damping ratio. Since the flapping frequency in flight is approximately from 9Hz to 15Hz, we set $\omega_n = 2\pi \cdot 8$, and chose $\zeta = 0.8$ according to the simulation performance.

As shown in Fig. 13, the oscillation induced by the flapping wings can be filtered by the designed filter. According to our observation in both simulations and experiments, implementing the corresponding filtered signal as the controller feedback can modify the robot flight performance.

B. Attitude Tracking

Stable attitude tracking is one of the prerequisites for deploying other flapping wing robot tasks. The basic idea of our developed attitude tracking controller originates in [33]. Implementing averaging method, the flapping wing attitude controller is to solve the rigid body attitude tracking problem on $\text{SO}(3)$, where the attitude representation complexities and ambiguities can be avoided. The $\text{SO}(3)$ group is

$$\text{SO}(3) = \{R \in \mathbb{R}^{3 \times 3} \mid RR^T = \mathbf{I}_3, \det[R] = 1\}, \quad (13)$$

where $\det[\star]$ is the determinant of \star . The Lie algebra associated with $\text{SO}(3)$ is $\mathfrak{so}(3) = \{S \in \mathbb{R}^{3 \times 3} \mid S = -S^T\}$.

The control objective is to make the robot orientation following the desired attitude trajectory, which is shown as

$$\dot{R}_d = R_d \hat{\Omega}_d \quad (14)$$

where $\hat{\Omega}_d \in \mathbb{R}^3$ is the desired angular rotation velocity, $R_d \in \text{SO}(3)$ is the desired rotation matrix.

First of all, the attitude dynamics is

$$J\dot{\Omega} = \tau + \delta\tau - \Omega \times J\Omega \quad (15)$$

$$\dot{R} = R\hat{\Omega} \quad (16)$$

where $J \in \mathbb{R}^{3 \times 3}$ is the inertia matrix in the body fixed frame, the hat map $\hat{\star} : \mathbb{R}^3 \rightarrow \mathfrak{so}(3)$ maps an angular velocity vector to a skew symmetric matrix, such that $\hat{\star}_1 \star_2 = \star_1 \times \star_2$, $\Omega \in \mathbb{R}^3$ is the angular rotation velocity, $R \in \text{SO}(3)$ is the rotation matrix representing the robot attitude in the inertia frame, $\tau \in \mathbb{R}^3$ is the torque input, and $\delta\tau \in \mathbb{R}^3$ is the composition of the torque disturbances and actuator faults from model uncertainties and actuator misalignment.

The attitude error function is

$$\Psi(R, R_d) = \frac{1}{2} \text{tr}[G(I - R_d^T R)] \quad (17)$$

where $R_d \in \text{SO}(3)$ is the desired robot orientation in the inertia frame, $\text{tr}(\star)$ indicates the trace of \star , and $G \in \mathbb{R}^{3 \times 3}$ is a

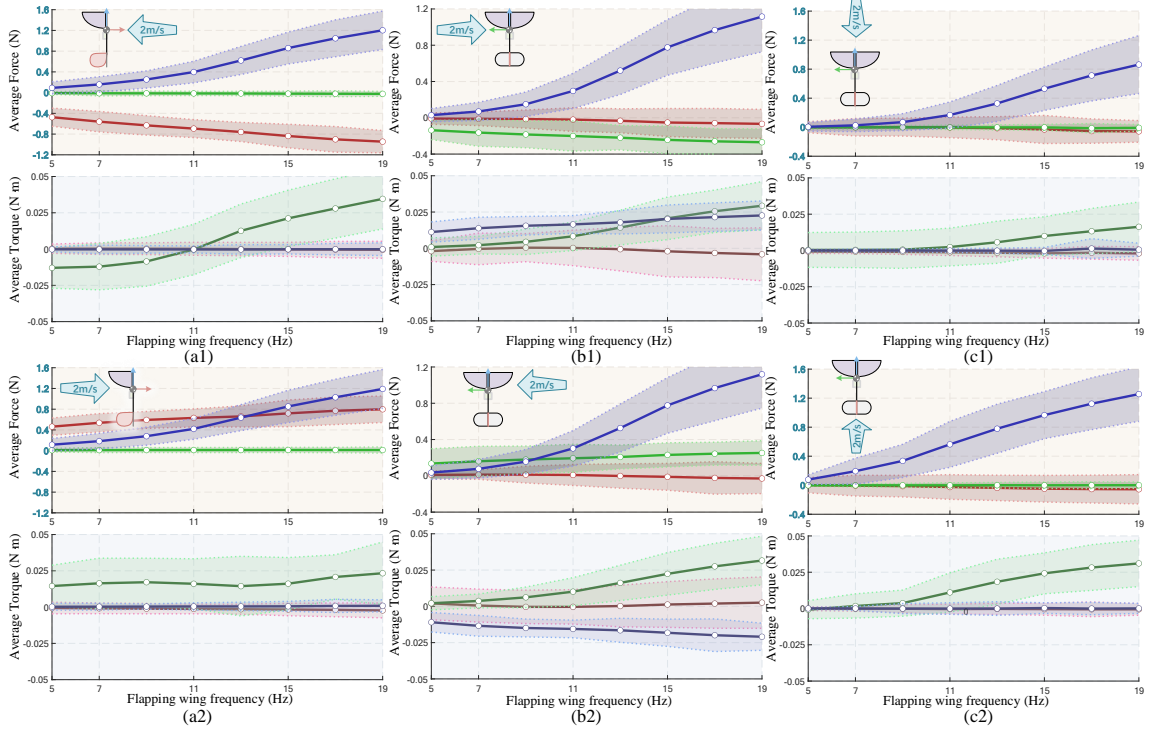


Fig. 12. Resultant average forces and torques generated by both wings and tails faced with different free flows. The shaded area width represents the oscillations that the periodic forces and torques exerted on the robot. The wings and tails are all set as neutral positions, corresponding to the situation of Fig. 10-e and 4 in Fig. 11. Detail free flows are sketched at the top left upper corner of each sub-figure. The forces and torques are all resolved in the body-fixed frame, right-handed system. Forces and torques along X-axis (ventral) are shown as red curves, Y-axis (left) green, Z-axis (cephalad) blue.

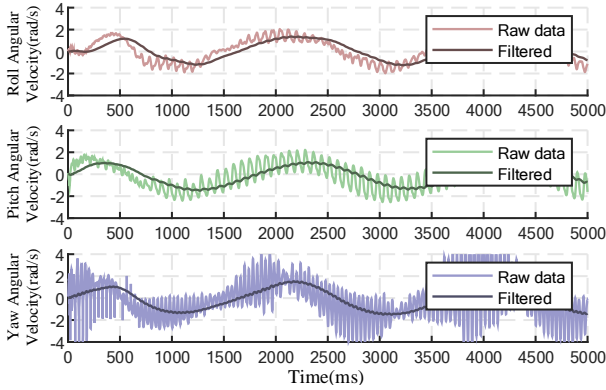


Fig. 13. Low-pass second order filter processing oscillating angular velocity signal in simulation.

positive definite, diagonal matrix. The attitude error $\Psi(R, R_d)$ dynamics is shown as

$$\frac{d}{dt}(\Psi(R, R_d)) = e_R^\top e_\Omega, \quad (18)$$

$$e_R = \frac{1}{2}(GR_d^\top R - R^\top R_d G)^\vee, \quad (19)$$

$$e_\Omega = \Omega - R^\top R_d \Omega_d, \quad (20)$$

$$\dot{e}_R = \frac{1}{2}(GR_d^\top R \hat{e}_\Omega + \hat{e}_\Omega R^\top R_d G)^\vee, \quad (21)$$

$$\dot{e}_\Omega = J^{-1}(-\Omega \times J\Omega + u + \delta\tau) - \alpha_d \quad (22)$$

where $(\star)^\vee : \mathfrak{so}(3) \rightarrow \mathbb{R}^3$ is the inverse map of $\hat{\star}$, $\alpha_d \in \mathbb{R}^3$ is the desired angular acceleration terms composition in the

current body-fixed frame, which is given by

$$\alpha_d = -\hat{\Omega}R^\top R_d \Omega_d + R^\top R_d \dot{\Omega}_d \quad (23)$$

Remark 1: The attitude error we use in this simulation has three unstable non-trivial critical points, and begin to decays after traveling $\pi/2$ along each curve corresponding to the geodesic spray at the initial point, which makes it less efficient in practical application. Hybrid attitude errors[24, 34] although with stronger system stability convergences in theory, however, owing to their partial discrete nature, will inevitably infuse detrimental non-smooth dynamic factors, which prevents these methods from being invoked in flapping wing robots usually requiring a relatively steady airflow condition.

Remark 2: Besides issues in conventional 6-DoF attitude control problems, the attitude tracking control problem of the flapping wing robot has the following two challenging aspects:

- 1) How to generate accurate τ which is strongly influenced by the flying state.
- 2) How to reject the undesired $\delta\tau$ disturbances as much as possible, by practical inputs and actuators.

There exist non-negligible differences between different robots and flight situations, such that exhaustive investigation of those maps is nearly impossible. Therefore we use the model reference adaptive method and robust controller design to attack this problem, which makes the controller more robust.

By synthesizing the attitude error and the angular velocity error, and combining them with adaptive and robust terms, the

control torque τ is given by

$$\tau = \underbrace{-k_R e_R - k_\Omega e_\Omega + v}_{\text{Feedback terms}} + \underbrace{\Omega \times \bar{J}\Omega + \bar{J}\alpha_d}_{\text{Feedforward terms}} \quad (24)$$

where $k_R, k_\Omega \in \mathbb{R}$ are positive constants, $e_R, e_\Omega \in \mathbb{R}^3$ are attitude error and angular velocity error, respectively, $v \in \mathbb{R}^3$ is the robust term, $\bar{J} \in \mathbb{R}^{3 \times 3}$ is the estimated inertia matrix. Since the inertia matrix usually can be approximately estimated, the update of the \bar{J} can be given by

$$\dot{\bar{J}} = \frac{k_J}{2} (-\alpha_d e_A^\top - e_A \alpha_d^\top + \Omega \Omega^\top \hat{e}_A - \hat{e}_A \Omega \Omega^\top - 2\sigma \bar{J}) \quad (25)$$

where e_A is the composition of attitude error and angular velocity error $e_A = e_\Omega + c e_R$, and $\sigma \in \mathbb{R}$ is the update damping rate. Inspired by the attitude control scheme reported in [33, 35], the robust term v can be designed in the following two ways, which are high frequency control, and synthesis of high frequency control and sliding mode control, respectively:

$$v_1 = -\frac{\delta_b^2 e_A}{\delta_b \|e_A\| + \varepsilon} \quad (26)$$

$$v_2 = -k_v \mathbf{sgn}(e_A) \|e_A\|^{\rho_v} - \frac{\delta_b^2 e_A}{\delta_b \|e_A\| + \varepsilon} \quad (27)$$

where $k_v, 0 < \rho_v < 1 \in \mathbb{R}$ are positive constants, $\mathbf{sgn}(\star) : \mathbb{R}^3 \rightarrow \mathbb{R}^3$ is the signal function which returns the signal of each element in the vector, which returns -1 for negative input, and 1 for positive, $\delta_b \in \mathbb{R}$ is the module bound of $\delta\tau$, and $\varepsilon \in \mathbb{R}$ is a relatively small constant to avoid singularity.

From phenomena PW-1, PR-2, and PF-1, we conclude that robot resultant force and torque are not only influenced by the flapping frequency but many other control commands and flying states, such that, even only along body-fixed frame Z-axis, the controller performance is not consistent at least under different flapping wing frequencies and desired attitudes. In the following attitude tracking control simulation, we use the actuation allocations provided in TABLE II and TABLE III, where the roll command is constrained within $[-\pi/4, \pi/4]$ to maintain the monotonicity. Similarly, equilibrium pitch positions are also restricted. Applying the aforementioned attitude tracking controller, the challenges highlighted in *Remark 2* can be basically overcome². However, in order to search a better attitude tracking controller, derived from (24), the following three controllers are implemented and further compared:

$$\begin{aligned} \tau_1 &= -k_R e_R - k_\Omega e_\Omega \\ \tau_2 &= -k_R e_R - k_\Omega e_\Omega + v_1 + \Omega \times \bar{J}\Omega + \bar{J}\alpha_d \\ \tau_3 &= -k_R e_R - k_\Omega e_\Omega + v_2 \end{aligned} \quad (28)$$

Basically, the controller τ_1 is similar to a proportional differential (PD) controller, the controller τ_2 is a robust adaptive controller, and controller τ_3 is a robust sliding mode controller. They all use the same attitude error function.

The comparison simulations are conducted with 6 different desired attitude trajectories:

²See source codes at https://github.com/Chainplain/Flapping_wing_Simu.

TABLE IV
ATTITUDE TRACKING PARAMETERS

Parameters	Values
Comparison controller τ_1	
attitude error coefficient, $G \in \mathbb{R}^3$	$\text{diag}([1 \ 1 \ 1]^\top)$
attitude error gain, $k_R \in \mathbb{R}$	2
angular velocity error gain, $k_\Omega \in \mathbb{R}$	0.2
Comparison controller, τ_2	
robust term v_1 first coefficient, $\delta_b \in \mathbb{R}$	0.2
robust term v_1 second coefficient, $\varepsilon \in \mathbb{R}$	0.1
adaptive term coefficient, $k_J \in \mathbb{R}$	0.1
adaptive term damping, $\sigma \in \mathbb{R}$	20
Proposed controller, τ_3	
robust term v_2 gain, $k_v \in \mathbb{R}$	0.15
robust term v_2 exponent, $\rho_v \in \mathbb{R}$	0.5

TABLE V
ATTITUDE TRACKING STEADY STATE PERFORMANCE
MEASURED IN Ψ

Tasks	Indicators	Control strategies		
		τ_1	τ_2	τ_3 Pro.
14-(a)	MAX	0.2315	0.1821	0.1060
	RMS	0.1043	0.0775	0.0475
14-(b1)	MAX	0.1211	0.1154	0.0565
	RMS	0.0459	0.0511	0.0286
14-(b2)	MAX	0.9031	1.0130	1.3708
	RMS	0.2808	0.3374	0.4465
14-(c)	MAX	0.1973	0.0876	0.1100
	RMS	0.0807	0.0481	0.0550
14-(d)	MAX	0.0866	0.0842	0.0510
	RMS	0.0358	0.0333	0.0221
14-(e)	MAX	0.2171	1.4197	0.1140
	RMS	0.0509	0.4208	0.0236

- (a) Start from Roll= 0 rad, Pitch= 0 rad, Yaw= 0 rad, with a constant desired angular velocity $[0.5\pi \ 0 \ 0]^\top$ rad/s.
- (b1) Start from Roll= 0 rad, Pitch= 0 rad, Yaw= 0 rad, with a constant desired angular velocity $[0 \ 0.5\pi \ 0]^\top$ rad/s.
- (b2) Start from Roll= 0 rad, Pitch= 0 rad, Yaw= 0 rad, with a constant desired angular velocity $[0 \ -0.5\pi \ 0]^\top$ rad/s.
- (c) Start from Roll= 0 rad, Pitch= 0 rad, Yaw= 0 rad, with a constant desired angular velocity $[0 \ 0 \ 0.5\pi]^\top$ rad/s.
- (d) Start from Roll= 0 rad, Pitch= 0 rad, Yaw= 0 rad, although with a time-varying sinusoidal angular velocity $[\frac{\pi}{2} \cos(\pi t) \ \frac{\pi}{2} \cos(\pi t) \ \frac{\pi}{2} \cos(\pi t)]^\top$.
- (e) The desired attitude trajectory presents step changes to the next value after every 2000 ms, with trivial desired angular velocity constantly set as $[0 \ 0 \ 0]^\top$ rad/s. The attitude values are given in ZYX-Euler angles, with the order as Roll, Pitch, Yaw: $[\frac{\pi}{2} \ 0 \ 0]^\top$, $[-\frac{\pi}{2} \ 0 \ 0]^\top$, $[0 \ \frac{\pi}{2} \ 0]^\top$, $[0 \ -\frac{\pi}{2} \ 0]^\top$, $[0 \ 0 \ -\frac{\pi}{2}]^\top$, $[0 \ 0 \ \frac{\pi}{2}]^\top$.

The frequency of the controller calculation loop is 100Hz, one tenth of the simulation computation frequency, which is practical to implement in real flight experiments. Simulation results are shown in Fig. 14. Parameters for these three controllers are all carefully tuned to achieve best performances, and are fixed for all 6 simulation tasks, which are clearly given in TABLE IV.

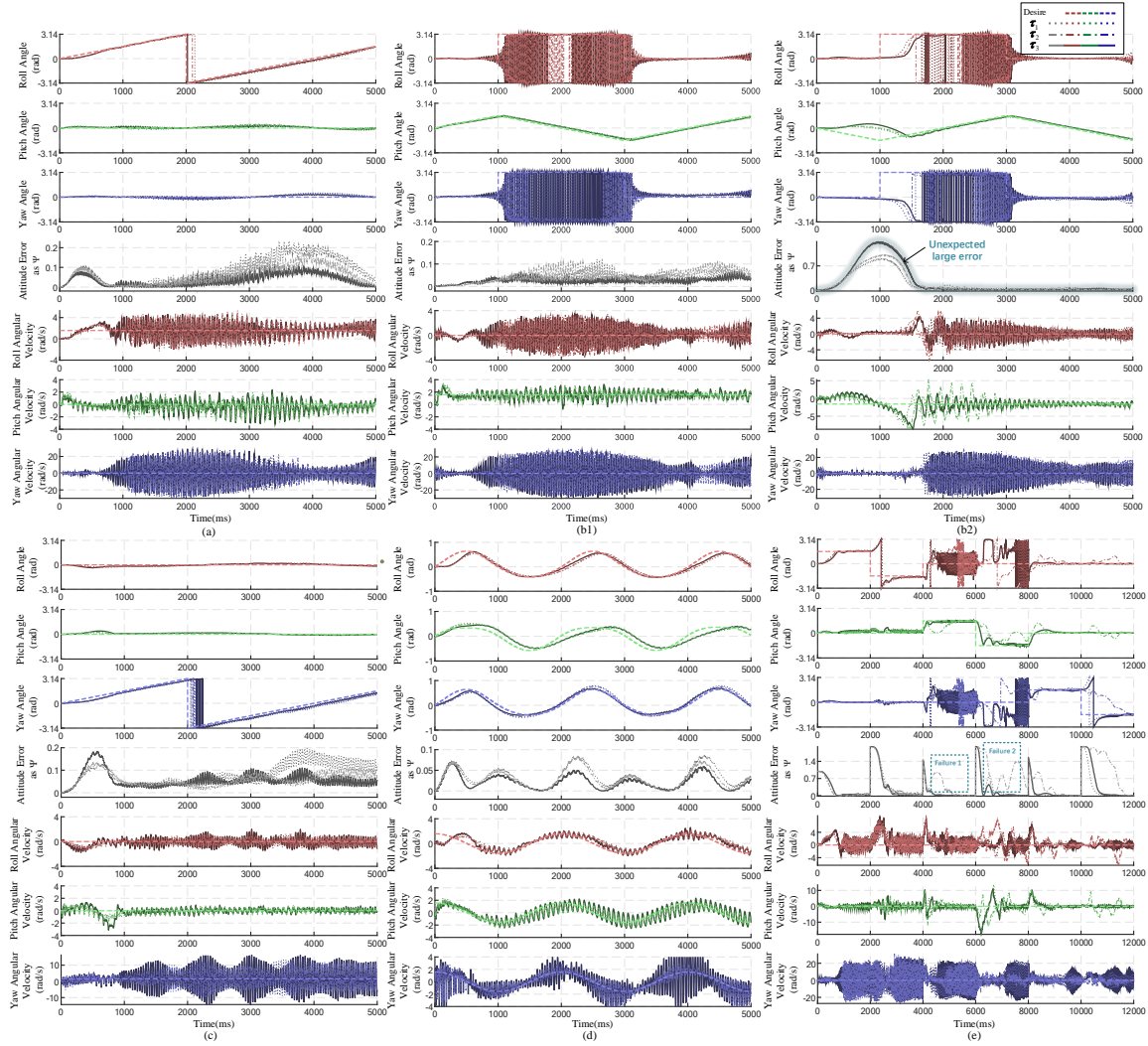


Fig. 14. Attitude tracking control simulations for three different control strategies, τ_1 , τ_2 , and τ_3 , in 6 different tasks. The attitude is represented in the ZYX-Euler angle for intuitive understanding, where roll (red) is the rotation around X-axis, pitch (green) is the rotation around Y-axis, yaw (blue) is the rotation around Z-axis. The overall attitude error is represented in the rotation error function Ψ , provided in (17).

Generally, the control strategy τ_3 superiors over the other two, concluding from different tasks attitude errors shown in Fig. 14. The control strategy τ_1 can barely satisfactorily achieve the attitude tracking task, which is however easy-to-use owing to its fewer parameters. The control strategy τ_2 can achieve satisfactory performance in steady flight although still having larger attitude error compared with τ_3 . Due to the integral essence of the controller τ_2 adaptive terms, implementing it in a flapping wing robot, which is oscillating and has no constant inertia matrix, system error accumulation may consequently induce unexpected behaviors, for example, the two failures shown in Fig. 14-(e). Based on these observations, τ_3 is selected as the attitude tracking control strategy for following tasks and applications. The steady-state performances are shown in TABLE V, which also indicate that controller τ_3 lead to better attitude trajectory tracking performance. In this table, MAX indicates the maximum attitude error ψ , RMS indicates the root mean square of ψ .

The following two behaviors in the attitude tracking tasks

are worthy to be deeply investigated.

- BAT-1: There are obvious angular velocity oscillations in almost all the tasks, especially for the yaw kinematics. Observing the variation trend of the angular velocities in Fig. 14-(a)(b1)(b2), it can be concluded that, when the robot is upright with relatively small free flow, the oscillation is moderate, and becomes drastic when the surrounded free flow is prominent, especially when the vehicle is faced with the circumstance as Fig. 12-(a1)(a2)(b1)(b2). As shown in the comparison simulation shown in Fig. 15, where the robot follows the attitude trajectory (a) equipped with controller τ_3 , the robot can achieve better performances with designed filter, with an error reduction larger than 60%. Moreover, the control inputs drastically oscillate without filtered feedback signals, which leads to larger control efforts, while the filtered ones are relatively steady, which is approximately 50% of the oscillation amplitude without the filter. In summary, the controller with 100Hz computation frequency, as well

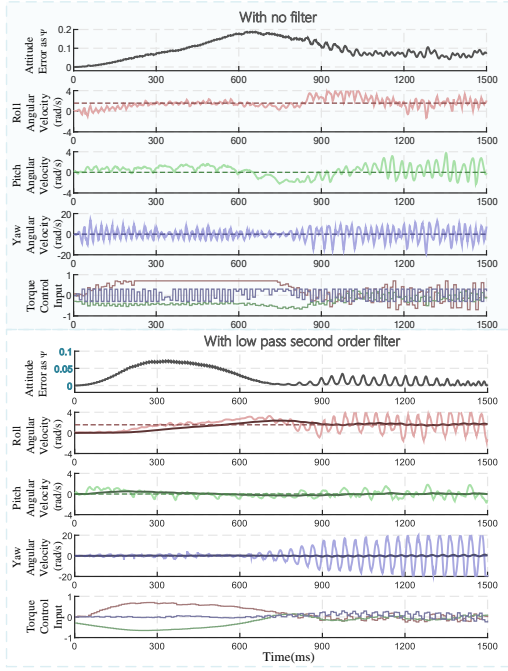


Fig. 15. Attitude tracking control performance without and with filter following desired attitude trajectory (a) equipped with control strategy τ_3 . The darker color curves represent the filtered signals, while the lighter curves are the raw signals.

as the practical actuators, *e.g.* servo motor usually only capable of achieving $\pi/3$ steering in at least 0.1 s, cannot actually be used to suppress the 13Hz frequency flapping induced oscillation. To this end, the oscillating angular velocity signal is hazardous in the feedback loop, which can drown the real effective feedback signal. On the other hand, after implementing the filter, the system being stable in the average sense, tolerable oscillation is certainly not taken into the feedback loop, therefore has no chance and is not necessary to be suppressed by the controller.

- BAT-2: The unexpected large errors occur in the simulation of all three controllers, when the vehicle tracks trajectory (b2), where the robot is basically back-flipping. Generally, the behavior difference between front-flip shown in Fig. 14-(b1) and back-flip shown in Fig. 14-(b2) is mainly due to PW-2. Let us further investigate the unexpected behaviors in 0-500 ms and 500-1000 ms, shown in Fig. 16, what we call *Descent phase* and *Front flip phase*, respectively. In *Descent phase*, the control input signal shown in Fig. 16 indicates that the robot has a similar situation demonstrated in Fig. 10-(h), where the robot suffers from PW-1. At the same time, the rotated thrust force makes the robot accelerate backward. After the acceleration, and reaching a backward velocity approximately to 1 m/s, the robot comes into *Front flip phase*. In this phase, PF-2 dominates, such that the robot pitches forward due to the airflow from the dorsal side. Combined with PW-2, the robot pitch is relatively fast. This pitch rotates the thrust back toward the opposite direction of gravity, making the robot ascend. In the

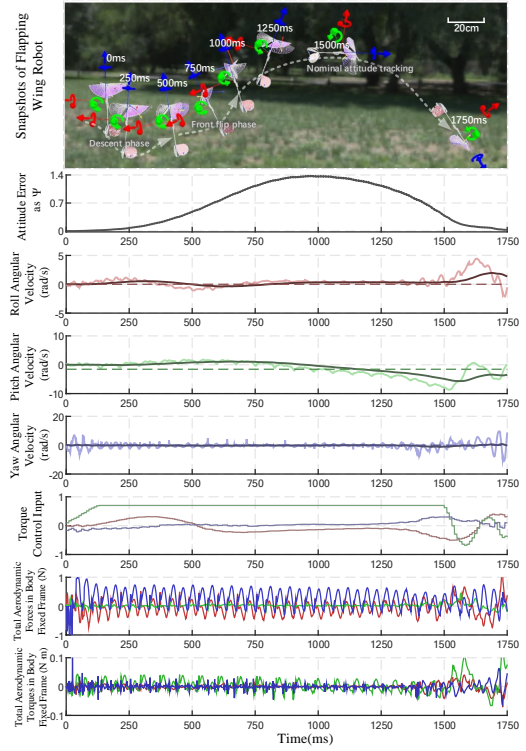


Fig. 16. Flapping wing robot behavior equipped with control strategy τ_3 , when tracking desired attitude trajectory (b2) where the unexpected large attitude tracking error emerges.

meantime, the backward thrust component reduces, and due to the resistance, the backward velocity decreases, thus PF-2 vanishes. Then the robot can finally generate negative pitch torque to track its desired attitude trajectory, and *Front flip phase* therefore ends.

C. Trajectory Tracking

Trajectory tracking in 3-dimensional Euclidean space is essential to explore the vehicle dynamics feasibility in the acrobatic flight, as well as the vehicle robustness in conventional flight. The control objective is to make the robot position following the desired translational trajectory, which is

$$\dot{\mathbf{p}}_d = \mathbf{v}_d \quad (29)$$

where $\mathbf{v}_d \in \mathbb{R}^3$ is the desired translational velocity in the inertia frame, $\mathbf{p}_d \in \mathbb{R}^3$ is the desired 3-dimensional position.

The translational dynamics can be given as

$$m\dot{\mathbf{v}} = \mathbf{R} \cdot F_t \mathbf{e}_3 + \mathbf{R} \mathbf{F}_a(\mathbf{Z}_b) + \delta \mathbf{F} - m \mathbf{g} \mathbf{e}_3, \quad (30)$$

$$\dot{\mathbf{p}} = \mathbf{v}$$

where $m \in \mathbb{R}$ is the robot mass, $\mathbf{p}, \mathbf{v} \in \mathbb{R}^3$ are the translational position and velocity of the robot mass center represented in the inertia frame, respectively, $\mathbf{e}_3 = [0 \ 0 \ 1]^T \in \mathbb{R}^3$ represents the vertical direction in the inertia frame, $F_t \in \mathbb{R}$ is the aerodynamics force component along the cephalad direction generated by the flapping wings, $\mathbf{F}_a(\mathbf{Z}_b) \in \mathbb{R}^3$ is the remainder aerodynamics forces, $\mathbf{Z}_b = [\mathbf{F} \ \mathbf{v}^T \ \boldsymbol{\Omega}^T]^T \in \mathbb{R}^7$ is the composition of aerodynamics influence factors, all

resolved in the inertia frame, $\delta\mathbf{F} \in \mathbb{R}^3$ is the composition of the force disturbances and actuator faults from model uncertainties and actuator misalignment, $g \in \mathbb{R}$ represents the gravitational acceleration magnitude. According to the robot attitude dynamics, the virtual control inputs of the translational dynamics system are the rotation matrix R and the thrust F .

The translation error function is defined as

$$\mathbf{e}_p(t) = \mathbf{p}_d(t) - \mathbf{p}(t) \quad (31)$$

where $\mathbf{e}_p \in \mathbb{R}^3$ is the robot translational error.

The translational error dynamics is shown as

$$\begin{aligned} \dot{\mathbf{e}}_p &= \mathbf{v}_d - \mathbf{v}, \\ \mathbf{e}_v &:= \dot{\mathbf{e}}_p, \\ \dot{\mathbf{e}}_v &= \dot{\mathbf{v}}_d - \frac{1}{m}R(F_t\mathbf{e}_3) - \frac{1}{m}R\mathbf{F}_a(\mathbf{Z}_b) - \frac{1}{m}\delta\mathbf{F} + g\mathbf{e}_3 \end{aligned} \quad (32)$$

where $\mathbf{e}_v \in \mathbb{R}^3$ is the translational velocity error.

Remark 3: The position trajectory tracking control problem of the flapping wing robot has the following three challenges:

- 1) Available control inputs appearing as $\frac{1}{m}R \cdot F_t\mathbf{e}_3$ only possess comparable magnitude of $\frac{1}{m}R\mathbf{F}_a(\mathbf{Z}_b)$. And these two terms are coupled, indicating that when the robot attitude as the control input changes, the remainder aerodynamic forces will also change. Therefore, we have to utilize $\frac{1}{m}R\mathbf{F}_a(\mathbf{Z}_b)$ to achieve our control objective, instead of rejecting it. Since $\frac{1}{m}R\mathbf{F}_a(\mathbf{Z}_b)$ is nearly not possible to be accurately modeled, the imperative need is to efficiently estimate it online.
- 2) How to reject the undesired $\delta\mathbf{F}$ disturbances as much as possible, by practical inputs and actuators.
- 3) Recalling BAT-2, when the robot translational velocity is deviated from the robot cephalad direction and is simultaneously large in magnitude, the unexpected behavior will emerge. Therefore, the robot cephalad direction should be constrained within a time-varying domain depending on translational velocity direction resolved in the body-fixed frame, in order to maintain maneuverability.

Let us simplify the expression of (30) and (32). Taking $\frac{1}{m}R(F_t\mathbf{e}_3)$ as $\mathbf{u}_t \in \mathbb{R}^3$, $\frac{1}{m}R\mathbf{F}_a(\mathbf{Z}_b)$ as $\mathbf{f}_a(t) \in \mathbb{R}^3$, the positional dynamics can be rewritten as

$$m\dot{\mathbf{v}} = \mathbf{u}_t + m\mathbf{f}_a(t) + \delta\mathbf{F} - mg\mathbf{e}_3, \quad (33)$$

$$\dot{\mathbf{e}}_v = \dot{\mathbf{v}}_d - \mathbf{f}_a(t) - \frac{1}{m}\delta\mathbf{F} + g\mathbf{e}_3 - \mathbf{u}_t$$

Based on (33) and enlightened by [36], an extended state observer is used to attack the first challenge in *Remark 3*. Since only \mathbf{p} is observable, the observer is designed as

$$\dot{\mathbf{p}}_o = \mathbf{v}_o - G_p\sigma^{\frac{\rho_e+1}{2}}(\mathbf{p}_o - \mathbf{p}) \quad (34)$$

$$m\dot{\mathbf{v}}_o = \mathbf{u}_t - mg\mathbf{e}_3 - G_v\sigma^{\frac{\rho_e+1}{2}}(\mathbf{p}_o - \mathbf{p}) + \mathbf{z} \quad (35)$$

$$\dot{\mathbf{z}} = -G_z\sigma^{\rho_e}(\mathbf{p}_o - \mathbf{p}) \quad (36)$$

where $\mathbf{z} \in \mathbb{R}^3$ can be viewed as an estimation of $m\mathbf{f}_a(t) + \delta\mathbf{F}$, $\mathbf{p}_o \in \mathbb{R}^3$ and $\mathbf{v}_o \in \mathbb{R}^3$ are the estimations of \mathbf{p} and \mathbf{v} , respectively, $G_p, G_v, G_z \in \mathbb{R}^{3 \times 3}$ are positive definite, diagonal matrices, and $\sigma^{*1}(\star_2) : \mathbb{R} \times \mathbb{R}^3 \rightarrow \mathbb{R}^3$ is a vector function, which implements the operation $\text{sgn}(|\star_{2i}|) |\star_{2i}|^{\star_1}$ on

each entry \star_{2i} of vector \star_2 , then sequentially connect obtained results as the output vector, $0 < \rho_e < 1 \in \mathbb{R}$ is a positive constant. It is noteworthy that, the robot velocity is not directly available, such that its estimation \mathbf{v}_o is used as the feedback.

Then we use the sliding mode robust control technique to overcome the second challenge in *Remark 3*. The control law is developed as

$$\begin{aligned} \mathbf{u}_{t1} &= \underbrace{K_s\sigma^{\rho_s}(s) + K_{ep}\tanh(K_p\mathbf{e}_p) + K_{ev}\mathbf{e}_v + K_{eI}Re_I}_{\text{Feedback terms}} \\ &\quad + \underbrace{\dot{\mathbf{v}}_d - \frac{1}{m}\mathbf{z} + g\mathbf{e}_3}_{\text{Feedforward terms}} \end{aligned} \quad (37)$$

where $s = c_s\tanh(K_p\mathbf{e}_p) + K_v\mathbf{e}_v \in \mathbb{R}^3$, $\mathbf{e}_I \in \mathbb{R}^3$ is the integral feedback considering both velocity and positional errors in the body-fixed frame, updated by $\dot{\mathbf{e}}_I = \text{proj}_{e_{Ib}}(R^\top(K_{Ip}\mathbf{e}_p + K_{Iv}\mathbf{e}_v))$ and $\mathbf{e}_p = \mathbf{p}_d - \mathbf{p}_o$, $\mathbf{e}_v = \mathbf{v}_d - \mathbf{v}_o \in \mathbb{R}^3$ are the position and velocity errors computed by the filtered signal, respectively, $\text{proj}_{e_{Ib}}(\star) : \mathbb{R}^3 \rightarrow \mathbb{R}^3$ is the projection function which constrains \mathbf{e}_I in predefined bound e_{Ib} . and $K_s, K_p, K_v, K_{ep}, K_{ev}, K_{eI}, K_{Ip}, K_{Iv} \in \mathbb{R}^{3 \times 3}$ are positive definite, diagonal matrices, $c_s \in \mathbb{R}$ is a positive constant. The saturation function $\tanh(\star) : \mathbb{R}^3 \rightarrow \mathbb{R}^3$ is a vector function, which implements the hyperbolic tangent function operation $\tanh(\star)$ on each entry \star of vector \star , and sequentially connects their results, moreover, $0 < \rho_s < 1 \in \mathbb{R}$ is a positive constant. The saturation function is implemented to avoid large position errors overwhelming other signals.

D. Desired Attitude Trajectory Generation

The nominal virtual input \mathbf{u}_t can be composed of the thrust magnitude and orientation. Based on Rodrigues' rotation formula, the desired orientation without rotation around Z-axis in the body-fixed frame, $R_{d\setminus Z} \in SO(3)$, can be developed as

$$R_{d\setminus Z} = I + \hat{\mathbf{k}} + \frac{1-c}{s^2 + \varepsilon_k} \hat{\mathbf{k}}^2, \quad (38)$$

$$\mathbf{k} = \mathbf{e}_3 \times \bar{\mathbf{u}}_t, \quad c = \mathbf{e}_3 \cdot \bar{\mathbf{u}}_t, \quad s = \|\mathbf{k}\|, \quad \bar{\mathbf{u}}_t = \mathbf{u}_t / \|\mathbf{u}_t\|$$

where $\mathbf{k} \in \mathbb{R}^3$ can be viewed as the rotation axis multiplied with sine value $s \in \mathbb{R}$ of the rotation angle, $\hat{\mathbf{k}} \in \mathbb{R}^{3 \times 3}$ is the skew symmetric matrix transformed from \mathbf{k} , $\varepsilon_k \in \mathbb{R}^+$ is a small positive constant to avoid singularity, $\bar{\mathbf{u}}_t \in \mathbb{R}^3$ is the normalized \mathbf{u}_t , $c \in \mathbb{R}$ is the cosine value of the rotation angle. To a certain extent, the rotation around Z-axis in the body-fixed frame is free in composing \mathbf{u}_t , whose rotation matrix conformed to the following restriction

$$R_Z(\alpha) = \begin{bmatrix} \cos \alpha & -\sin \alpha & 0 \\ \sin \alpha & \cos \alpha & 0 \\ 0 & 0 & 1 \end{bmatrix}$$

where $\alpha \in \mathbb{R}$ is the rotation angle. Then the desired orientation as a rotation matrix is given by

$$R_d = R_{d\setminus Z}R_Z \quad (39)$$

Recalling that there exists velocity term Ω_d in the error dynamics (20), the continuity of $R_{d\setminus Z}R_Z$ above the second

differential is indispensable, which is addressed by alternatively using the signal from a differential tracker

$$\begin{aligned} \dot{R}_f &= R_f \hat{\Omega}_f \\ \dot{\Omega}_f &= -K_{\omega f} \Omega_f - k_{Rf} e_{Rf} \\ e_{Rf} &= \frac{1}{2} (G_f R_d^\top R_f - R_f^\top R_d G_f)^\vee \end{aligned} \quad (40)$$

where $k_{Rf} \in \mathbb{R}$ is positive constant, and $K_{\omega f}, G_f \in \mathbb{R}^3$ are positive definite, diagonal matrices, $R_f \in SO(3)$ is the filtered rotation matrix, $\Omega_f \in \mathbb{R}^{3 \times 3}$ is the filtered angular velocity, and $e_{Rf} \in \mathbb{R}^3$ is the attitude error between the filtered and desire. Furthermore, the thrust is given by $m \|\mathbf{u}_t\|$. And we can use the robot hovering flight flapping wing frequency to translate the thrust into flapping frequency, considering that the flapping frequency is linear with respect to the thrust, where the modeling error can be handled by the robust controller:

$$f_t(t) = \frac{f_{\text{hover}}}{g} \|\mathbf{u}_t(t)\|$$

where $f_{\text{hover}} \in \mathbb{R}^+$ is the flapping frequency at hovering. In order to maintain the pitch and yaw torque generation capability, the flapping wing frequency is restricted in [9, 15] Hz.

Since the robot is susceptible to wind direction with limited attitude maneuverability, as illustrated in PF-2 and PF-3, the planning of the R_Z , in comparison to quadrotors and symmetric flapping wing robots, suffers more restrictions. Similar to the design of $R_{d\setminus Z}$, we can construct the desire rotation R_Z in the following way:

$$R_Z = I + \hat{\mathbf{k}}_z + \frac{1 - c_z}{s_z^2} \hat{\mathbf{k}}_z^2, \quad (41)$$

$$\mathbf{k}_z = \mathbf{d}_T \times \bar{\mathbf{v}}_{xy}, \quad c_z = \mathbf{d}_T \cdot \bar{\mathbf{v}}_{xy}, \quad s_z = \|\mathbf{k}\|, \quad \bar{\mathbf{v}}_{xy} = \mathbf{v}_{xy} / \|\mathbf{v}_{xy}\|$$

where $\mathbf{v}_{xy} = [v_{dx} \ v_{dy} \ 0]^\top \in \mathbb{R}^3$ is the desired velocity direction in inertia frame XY-plane, while $\mathbf{v}_d = [v_{dx} \ v_{dy} \ v_{dz}]^\top$, $\mathbf{d}_T \in \mathbb{R}^3$ is the direction aligned to the desired velocity direction in the XY-plane, which can be designed to determine the flight mode.

Remark 4: Expecting to perform aggressive flights, it is noteworthy that the observer (34-36) and the filter (40) are necessary to be updated in a higher frequency than the controller. Furthermore, the filter (40) is actually running discretely, thus normalization of the rotation matrix is needed, whose accuracy is also dependent on high-frequency update. Therefore, the observer and the filter are updated at 1000Hz.

In conclusion, the position controller, attitude controller, external state observer, and filter are synthesized into the trajectory controller, whose overall diagram is shown in Fig. 17

E. Autonomous Flight Simulation

The flapping wing robot autonomous flight with the proposed control scheme is conducted in our simulation platform. The attitude tracking controller τ_3 shown in (28) is used in the simulation. For comparison, the following trajectory tracking controller are also implemented.

$$\mathbf{u}_{t2} = K_{ep2} \tanh(K_{p2} e_p) + K_{ev2} e_v \quad (42)$$

$$\mathbf{u}_{t3} = K_{s3} \text{sgn}(s_3) + K_{ep3} e_p + K_{ev3} e_v + \dot{\mathbf{v}}_d + g \mathbf{e}_3 \quad (43)$$

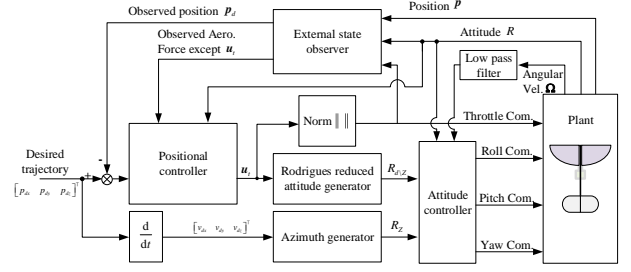


Fig. 17. Flapping wing robot trajectory tracking control block diagram.

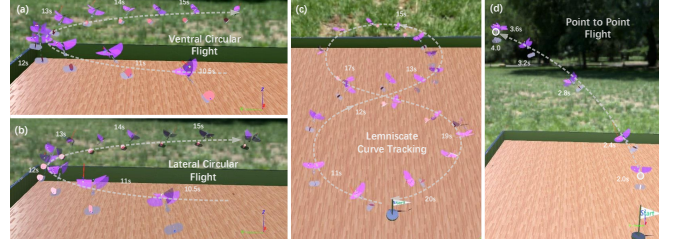


Fig. 18. Snapshots of different trajectory tracking tasks: (a) ventral circular flight, (b) lateral circular flight, (c) Lemniscate curve tracking, (d) point-to-point flight.

where $s_3 = e_p + K_{v3} e_v$, and $K_{ep2}, K_{p2}, K_{ev2}, K_{s3}, K_{ep3}, K_{ev3}, K_{v3} \in \mathbb{R}^{3 \times 3}$ are positive definite, diagonal matrices. Generally, the control law \mathbf{u}_{t2} can be classified as the model reference saturated PD controller, which is similar to the position controller proposed in [11], and the control law \mathbf{u}_{t3} can be seen as a sliding mode controller, which is analogue to the controller proposed in [37].

The simulations are performed with 4 different tasks, namely ventral circular flight (v-Cir.), lateral circular flight (l-Cir.), Lemniscate curve tracking (Lem.) and point-to-point flight (P2P), where time is measured in seconds:

$$\begin{aligned} \text{Cir. : } & \begin{cases} p_{dx}(t) = 2 - 2 \cos(0.2\pi t) \\ p_{dy}(t) = 2 \sin(0.2\pi t) \\ p_{dz}(t) = 0 \end{cases} \\ \text{Lem. : } & \begin{cases} p_{dx}(t) = 2 - 2 \cos(0.2\pi t) / (1 + \sin^2(0.2\pi t)) \\ p_{dy}(t) = 2 \sin(0.2\pi t) / (1 + \sin^2(0.2\pi t)) \\ p_{dz}(t) = 0 \end{cases} \\ \text{P2P : } & \begin{cases} p_{dx}(t) = 0 \\ p_{dy}(t) = 0 \\ p_{dz}(t) = 0 \end{cases}, t \leq 2 \quad \begin{cases} p_{dx}(t) = 2 \\ p_{dy}(t) = 2 \\ p_{dz}(t) = 2 \end{cases}, 2 < t \leq 8 \\ & \begin{cases} p_{dx}(t) = 0 \\ p_{dy}(t) = 0 \\ p_{dz}(t) = 0 \end{cases}, t > 8 \end{aligned}$$

where $\bar{\mathbf{p}}_d(t) = [p_{dx}(t) \ p_{dy}(t) \ p_{dz}(t)]^\top$ m is fed into the trajectory tracking controller as the desired trajectory. In tasks of v-Cir., Lem., and P2P, \mathbf{d}_T is set as $[1 \ 0 \ 0]^\top$, while in l-Cir., \mathbf{d}_T is set as $[0 \ 1 \ 0]^\top$. The robot snapshots in stable tracking with respect to these trajectories are shown in Fig. 18. Parameters for these three controllers are tuned to achieve their own optimal performances, and are fixed for all 4 simulation tasks, which are collectively shown in TABLE VI.

TABLE VI
 TRAJECTORY TRACKING PARAMETERS

Parameters	Values
Proposed controller \mathbf{u}_{t1}	
robust term gain, $K_s \in \mathbb{R}^{3 \times 3}$	$\text{diag}([1 \ 1 \ 1]^T)$
positional error gain in robust term before saturation, $K_p \in \mathbb{R}^{3 \times 3}$	$0.8 \text{ diag}([1 \ 1 \ 1]^T)$
velocity error gain in robust term, $K_v \in \mathbb{R}^{3 \times 3}$	$0.5 \text{ diag}([1 \ 1 \ 1]^T)$
positional error gain before saturation, $K_{ep} \in \mathbb{R}^{3 \times 3}$	$10 \text{ diag}([1 \ 1 \ 1]^T)$
velocity error gain, $K_{ev} \in \mathbb{R}^{3 \times 3}$	$0.5 \text{ diag}([1 \ 1 \ 1]^T)$
integral error gain, $K_{eI} \in \mathbb{R}^{3 \times 3}$	$0.01 \text{ diag}([1 \ 1 \ 1]^T)$
positional error gain in integral term, $K_{Ip} \in \mathbb{R}^{3 \times 3}$	$0.8 \text{ diag}([1 \ 1 \ 1]^T)$
velocity error gain in integral term, $K_{Iv} \in \mathbb{R}^{3 \times 3}$	$0.5 \text{ diag}([1 \ 1 \ 1]^T)$
positional error gain in robust term after saturation, $c_s \in \mathbb{R}$	2
robust term exponent, $\rho_s \in \mathbb{R}$	0.5
ESO used in \mathbf{u}_{t1}	
first order observer gain, $G_p \in \mathbb{R}^{3 \times 3}$	$20 \text{ diag}([1 \ 1 \ 1]^T)$
second order observer gain, $G_v \in \mathbb{R}^{3 \times 3}$	$10 \text{ diag}([1 \ 1 \ 1]^T)$
extended state observer gain, $G_z \in \mathbb{R}^{3 \times 3}$	$5 \text{ diag}([1 \ 1 \ 1]^T)$
ESO exponent, $\rho_e \in \mathbb{R}$	0.5
Comparison controller \mathbf{u}_{t2}	
positional error gain after saturation, $K_{ep2} \in \mathbb{R}^{3 \times 3}$	$10 \text{ diag}([1 \ 1 \ 1]^T)$
positional error gain before saturation, $K_{p2} \in \mathbb{R}^{3 \times 3}$	$0.8 \text{ diag}([1 \ 1 \ 1]^T)$
velocity error gain, $K_{ev2} \in \mathbb{R}^{3 \times 3}$	$\text{diag}([1 \ 1 \ 1]^T)$
Comparison controller \mathbf{u}_{t3}	
sliding mode robust term gain, $K_{s3} \in \mathbb{R}^{3 \times 3}$	$0.5 \text{ diag}([1 \ 1 \ 1]^T)$
velocity error gain in robust term, $K_{v3} \in \mathbb{R}^{3 \times 3}$	$0.5 \text{ diag}([1 \ 1 \ 1]^T)$
positional error gain, $K_{ep3} \in \mathbb{R}^{3 \times 3}$	$8 \text{ diag}([1 \ 1 \ 1]^T)$
velocity error gain, $K_{ev3} \in \mathbb{R}^{3 \times 3}$	$0.5 \text{ diag}([1 \ 1 \ 1]^T)$

Based on the observation of the simulation results shown in Fig. 19, and further the steady state performance shown in TABLE VII, we can conclude that the control strategy \mathbf{u}_{t1} significantly superiors over the other two comparisons, with at least 25% RMS drop, and approximately 50% RMS drop in average. Furthermore, comparing the simulation results between (a) and (b), (a) and (c), we can find that the tracking performance deteriorates in lateral flight, or when tracking other large curvature trajectories. When the desired trajectory is discontinuous, as show in (d), controllers can barely achieve the tracking mission, which reveals that trajectory planning is needed, however, beyond the scope of this paper.

V. EXPERIMENTAL VALIDATION

In order to validate the proposed flapping wing robot simulation platform, we conduct a series of practical real

 TABLE VII
 TRAJECTORY TRACKING STEADY STATE PERFORMANCE MEASURED IN POSITIONAL ERROR

Tasks	Indicators	Control strategies		
		\mathbf{u}_{t1} Pro.	\mathbf{u}_{t2}	\mathbf{u}_{t3}
(a) v-Cir.	MAX	0.2314 m	1.0235 m	0.8512 m
	RMS	0.1226 m	0.9400 m	0.7681 m
(b) l-Cir.	MAX	0.3436 m	0.7466 m	2.0142 m
	RMS	0.1660 m	0.6722 m	0.8515 m
(c) Lem.	MAX	0.8334 m	0.9645 m	0.8016 m
	RMS	0.4433 m	0.8346 m	0.6789 m
(d) P2P	MAX	0.9644 m	2.4993 m	1.2115 m
	RMS	0.3499 m	0.7726 m	0.4674 m

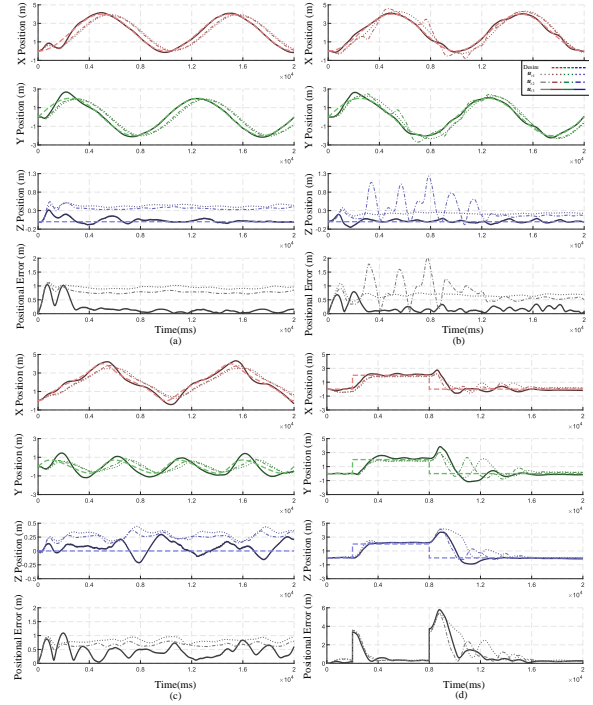


Fig. 19. Trajectory tracking simulation results with 3 different control laws \mathbf{u}_{t1} , \mathbf{u}_{t2} and \mathbf{u}_{t3} , within 4 different positional trajectories : (a) ventral circular flight, (b) lateral circular flight, (c) Lemniscate curve tracking, (d) point-to-point flight.

flights. These experiments are performed under a Qualisys motion capture arena with 48 Arqus A12 cameras online. And a self-made 29g flapping wing robot possessing the identical configuration as the robot in the above simulations, is tested. The controller is programmed with Python in a multithread fashion, which endows it with expansibility, and can be safely run on a non-real-time system with a desired frequency of 100Hz. We attach 4 tracking mark points to the vehicle to estimate its attitude and position. The ‘‘DIY multi-protocol TX module’’ is used to transmit the control signals to the receiver, with a desired frequency of 50Hz. Since the system is non-real-time, the computing and transmitting frequencies are not precisely fixed at their desired ones. To this end, an analyzing thread is performed to analyze other thread frequencies online, and further fine-tune the computations involved time. The overall platform constitution is shown in Fig. 20.

The attitude stabilization experiments are performed with

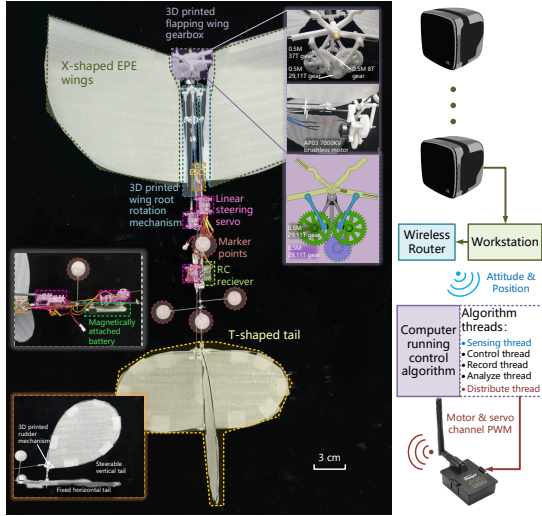


Fig. 20. Flapping wing robot platform used in real flight experiment.

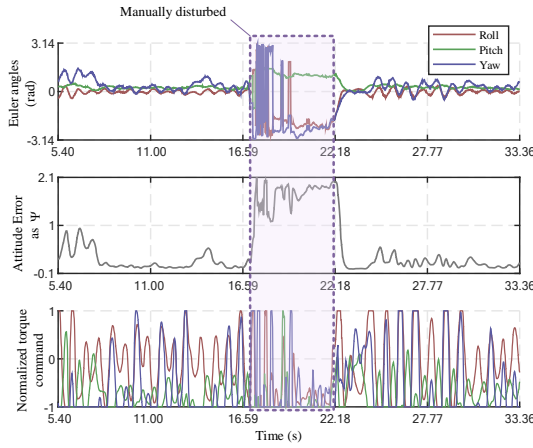


Fig. 21. Flapping wing robot behavior equipped with control strategy τ_3 when stabilizing the robot to the desired attitude $\text{diag}([1 \ 1 \ 1]^T)$ in real flight experiment.

three different attitude controllers (28) with the desired attitude set as $\text{diag}([1 \ 1 \ 1]^T)$ ³. We use exactly the same control laws τ_3 and parameters provided in TABLE V except that output channel mappings are modified to adapt the RC receiver signal, using pulse width modulation technique (PWM). Therefore, we can directly check the simulation accuracy by comparing simulation/experiment results.

The experimental result obtained from a flight experiment is shown in Fig. 21. Based on the result, we can conclude that the proposed control law and parameters tuned in simulations can also be directly applied to the real flight with satisfactory performance. Specifically, the robot can adjust its attitude to the desired attitude, even after manually disturbing, which manifests system robustness. Furthermore, comparing with the simulation in 14-(e), we can find that the stabilizing time length in real flight experiments is similar to that in simulations.

³See https://github.com/Chainplain/Flapping_wing_TrajControlExperiment.

TABLE VIII
ATTITUDE STABILIZATION EXPERIMENT
STEADY STATE PERFORMANCE MEASURED IN Ψ

Indicators	Control strategies		
	τ_1	τ_2	τ_3 Pro.
MAX	0.4359	0.5331	0.2730
RMS	0.1250	0.2012	0.0941

Further comparison experiments are also conducted to corroborate the controller comparison results based on simulations. The comparison experiments result are shown in TABLE VIII. And, we find that the proposed controller also has better steady state performance than the other two, which validates the conclusion made by observing our simulation results.

VI. CONCLUSION

In this paper, we propose a novel robotic application-oriented flapping wing simulation platform. The platform is used to investigate the dynamic characteristic, such as the passive wing rotation and the wing-tail interaction phenomena. The trade-off between computation simplicity and fidelity is carefully dealt with, such that most robotic tasks can be simulated, meanwhile, in application-oriented simulations, the forces and torques actuated on each blade element can be obtained, which are both rarely achieved in existing simulation tools. Moreover, the attitude tracking control and the positional trajectory tracking tasks as well as their comparison tests are successfully performed on the proposed simulation platform. Last but not least, the real flight experiments are also completed successfully by directly applying exactly the same algorithms and parameters used in simulations, which indicates that, to some extent, the gap between flapping wing flight simulation and real robotic application flight is bridged. In the future, we will fully use this simulation tool to develop flapping wing robots with various scales and configurations. Learning based and data driven algorithms will also be applied to explore their extensibility and generalization performance.

APPENDIX A

FLAPPING WING STATISTICS OF OSCILLATIONS

The imperative need of characterizing the flapping wing oscillation in the sense of dynamics impels us to define an intuitive overall statistic.

First of all, periodically computed variance (PV) and standard deviation (PSD) are not suitable, because flapping wing forces and torques with large PV and PSD may also induce relatively steady body kinematics. For example, higher flapping frequency will generate smoother dynamics, however, it does not necessarily lead to lower PV or PSD as expected.

To this end, we propose a novel statistic for flapping wing aerodynamic forces and torques that can capture the oscillating dynamics. Since the forces and torques are not definitely periodic, consider following the general averaging theory first.

Theorem 1 (General averaging [38]): Consider two dynamics system with the same initial condition:

$$\dot{x} = \varepsilon f(x, t), \quad x(0) = a \quad (44)$$

where $\mathbf{x}, \mathbf{a} \in D \subset \mathbb{R}^n$ and $\mathbf{f}(\star_1, \star_2) : \mathbb{R}^n \times \mathbb{R} \rightarrow \mathbb{R}^n$.

$$\mathbf{z} = \varepsilon \bar{\mathbf{f}}(\mathbf{z}), \quad \mathbf{z}(0) = \mathbf{a} \quad (45)$$

where $\mathbf{z} \in D \subset \mathbb{R}^n$ and $\mathbf{f}(\star) : \mathbb{R}^n \rightarrow \mathbb{R}^n$.

Suppose the following two issues are satisfied.

- 1) $\mathbf{f}(\star_1, \star_2)$ is a KBM-vector field with average $\bar{\mathbf{f}}(\star)$ and order function $\delta(\varepsilon)$.
- 2) Trajectory $\mathbf{z}(t)$ belongs to an interior set of D on the time scale $1/\varepsilon$.

Then the two systems satisfy

$$\mathbf{x}(t) - \mathbf{z}(t) = \mathcal{O}(\sqrt{\delta(\varepsilon)}) \quad (46)$$

as $\varepsilon \rightarrow 0$ on the time scale $1/\varepsilon$, where

$$\delta(\varepsilon) = \sup_{\mathbf{x} \in D} \sup_{t \in [0, L/\varepsilon]} \varepsilon \left\| \int_0^t [\mathbf{f}(\mathbf{x}, s) - \bar{\mathbf{f}}(\mathbf{x})] ds \right\| \quad (47)$$

Immediately, according to this difference bound between the oscillating system and the averaged system, we can design the statistic describing flapping wing oscillation degree as (11).

REFERENCES

- [1] S. Tijmons, G. de Croon, B. Remes, C. De Wagter, and M. Mulder, "Obstacle Avoidance Strategy using Onboard Stereo Vision on a Flapping Wing MAV," *IEEE Trans. Robot.*, vol. 33, no. 4, pp. 858-874, Aug. 2017.
- [2] M. Karásek, F. T. Muijres, C. De Wagter, B. D. Remes, and G. C. de Croon, "A tailless aerial robotic flapper reveals that flies use torque coupling in rapid banked turns," *Science*, vol. 361, no. 6407, pp. 1089-1094, Sep. 2018.
- [3] Z. Tu, F. Fei, J. Zhang and X. Deng, An At-Scale Tailless Flapping-Wing Hummingbird Robot. I. Design, Optimization, and Experimental Validation, *IEEE Trans. Robot.*, vol. 36, no. 5, pp. 1511-1525, Oct. 2020.
- [4] J. P. Rodríguez-Gómez, R. Tapia, J. Paneque, P. Grau, A. Eguíluz, J. Martínez-de Dios, and A. Ollero, The GRIFFIN Perception Dataset: Bridging the Gap Between Flapping-Wing Flight and Robotic Perception, *IEEE Rob. Autom. Lett.*, vol. 6, no. 2, pp. 1066-1073, April 2021.
- [5] R. Zufferey, J. Tormo-Barbero, M. Mar Guzmán, F. Maldonado, E. Sanchez-Laulhe, P. Grau, M. Pérez, J. Acosta, and A. Ollero, "Design of the High-Payload Flapping Wing Robot E-Flap," *IEEE Rob. Autom. Lett.*, vol. 6, no. 2, pp. 3097-3104, Apr. 2021
- [6] A. Chen, B. Song, Z. Wang, D. Xue and K. Liu, "A Novel Actuation Strategy for an Agile Bioinspired FWAV Performing a Morphing-Coupled Wingbeat Pattern," *IEEE Trans. Robot.*, 2022, Early access doi: 10.1109/TRO.2022.3189812.
- [7] X. Wu, W. He, Q. Wang, T. Meng, X. He and Q. Fu, "A Long-Endurance Flapping-Wing Robot based on Mass Distribution and Energy Consume Method," *IEEE Trans. Ind. Electron.*, 2022, Early access doi: 10.1109/TIE.2022.3213905.
- [8] F. Fei, Z. Tu, Y. Yang, J. Zhang and X. Deng, "Flappy Hummingbird: An Open Source Dynamic Simulation of Flapping Wing Robots and Animals," in Proc. *IEEE Inter. Conf. Rob. Auto.* pp. 9223-9229, Montreal, QC, Canada, 2019.
- [9] C. Orlowski and A. Girard, "Modeling and Simulation of Nonlinear Dynamics of Flapping Wing Micro Air Vehicles," *AIAA J.*, vol. 49, no. 5, pp. 969-981, Apr. 2011.
- [10] R. Lopez-Lopez, V. Perez-Sanchez, P. Ramon-Soria, A. Martín-Alcántara, R. Fernandez-Feria, B. Arrue, and A. Ollero "A Linearized Model for an Ornithopter in Gliding Flight: Experiments and Simulations," in Proc. *IEEE Inter. Conf. Rob. Auto.* pp. 7008-7014, Paris, France, 2020.
- [11] W. He, X. Mu, L. Zhang, and Y. Zou "Modeling and trajectory tracking control for flapping-wing micro aerial vehicles," *IEEE/CAA J. Auto. Sin.*, vol. 8, no. 1, pp. 148-156, Jan. 2021.
- [12] S. P. Sane and M. H. Dickinson. "The aerodynamic effects of wing rotation and a revised quasi-steady model of flapping flight," *Journal of experimental biology*, vol. 205, no. 8, pp. 1087-1096, Jan. 2002.
- [13] S. A. Ansari, R. Zbikowski, and K. Knowles, "Aerodynamic modelling of insect-like flapping flight for micro air vehicles," *Prog. Aeronaut. Sci.*, vol. 42, no. 2, pp. 129-172, Feb. 2006.
- [14] X. Deng, L. Schenato, W. C. Wu, and S. Sastry. "Flapping flight for biomimetic robotic insects: Part I-system modeling," *IEEE Trans. Robot.*, vol. 22, no. 4, pp. 776-788, Aug. 2006.
- [15] Y. M. Chukewad and S. Fuller, "Yaw Control of a Hovering Flapping-Wing Aerial Vehicle With a Passive Wing Hinge," *IEEE Rob. Autom. Lett.*, vol. 6, no. 2, pp. 1864-1871, April 2021.
- [16] Y. Chen, S. Xu, Z. Ren and P. Chirarattananon, "Collision Resilient Insect-Scale Soft-Actuated Aerial Robots With High Agility," *IEEE Trans. Robot.*, vol. 37, no. 5, pp. 1752-1764, Oct. 2021.
- [17] H. Rifai, N. Marchand, and G. Poulin-Vittrant, "Bounded control of an underactuated biomimetic aerial vehicle-Validation with robustness tests," *Rob. Auton. Syst.*, vol. 60, no. 9, pp. 1165-1178, Sep. 2012.
- [18] W. He, T. Meng, X. He, and C. Sun, "Iterative Learning Control for a Flapping Wing Micro Aerial Vehicle Under Distributed Disturbances," *IEEE Trans. Cybern.*, vol. 49, no. 4, pp. 1524-1535, Apr. 2019.
- [19] A. A. Paranjape, S. J. Chung, and J. Kim, "Novel dihedral-based control of flapping-wing aircraft with application to perching," *IEEE Trans. Rob.*, vol. 29, no. 5, pp. 1071-1084, Oct. 2013.
- [20] Y. J. Lee, K. B. Lua, T. T. Lim, and K. S. Yeo, "A quasi-steady aerodynamic model for flapping flight with improved adaptability," *Bioinspiration & Biomimetics*, vol. 11, no. 3, pp. 1-27, Apr. 2016.
- [21] D. D. Chin and D. Lentink, "Flapping wing aerodynamics: from insects to vertebrates," *J. Exp. Biol.*, vol. 219, no. 7, pp. 920-932, Apr. 2016.
- [22] S. P. Sane, "The aerodynamics of insect flight," *J. Exp. Biol.*, vol. 206, no. 23, pp. 4191-4208, Dec. 2003.
- [23] H. V. Phan, H. C. Park, "Insect-inspired, tailless, hover-capable flapping-wing robots: Recent progress, challenges, and future directions," *Prog. Aeronaut. Sci.*, vol. 111, no. 2, pp. 1-21, Nov. 2019.
- [24] C. Qian, Y. Fang, Y. Li, "Quaternion-based Hybrid Attitude Control for an Under-actuated Flapping Wing Aerial Vehicle," *IEEE Trans. Mechatron.*, vol. 24, no. 5, pp. 2341 - 2352, Oct. 2019.
- [25] J. Wu, and M. Sun, "The influence of the wake of a flapping wing on the production of aerodynamic forces," *Acta Mechanica Sinica*, vol. 21, issue 5, pp.411-418, Oct. 2005.
- [26] C. P. Ellington "The novel aerodynamics of insect flight: applications to micro-air vehicles," *J. Exp. Biol.*, vol. 202, issue 23, pp.3439-3448, Dec. 1999.
- [27] J. Han, J. Kim, J. Chang, and J. Han. "An improved quasi-steady aerodynamic model for insect wings that considers movement of the center of pressure," *Bioinspiration & biomimetics*, vol. 10, issue 4: 046014, Jul. 2015.
- [28] Q. Wang, J. F. L. Goosen and F. van Keulen, "A predictive quasi-steady model of aerodynamic loads on flapping wings," *Journal of Fluid Mechanics*, vol. 200, no. 24, pp. 688-719, Aug. 2016.
- [29] S. F. Armanini, J. V. Caetano, C. C. De Visser, M. D. Pavel, G. C. H. E. De Croon and M. Mulder, "Modelling wing wake and tail aerodynamics of a flapping-wing micro aerial vehicle," *Int. J. Micro Air Veh.*, vol. 11, pp. 1-24, Mar. 2019.
- [30] Webots. <http://www.cyberbotics.com>. Commercial Mobile Robot Simulation Software.
- [31] S. Wang, B. Song, A. Chen, Q. Fu, and J. Cui, "Modeling and flapping vibration suppression of a novel tailless flapping wing micro air vehicle," *Chin. J. Aeronaut.*, vol. 35, no. 3, pp. 309-328, Mar. 2022.
- [32] Z. Tu, F. Fei, Y. Yang, J. Zhang, and X. Deng, "Realtime on-board attitude estimation of high-frequency flapping wing mavs under large instantaneous oscillation," in Proc. *IEEE Inter. Conf. Rob. Auto.* Brisbane, Australia, pp. 6806-6811, May. 2018.
- [33] T. Lee, "Robust Adaptive Attitude Tracking on SO(3) With an Application to a Quadrotor UAV," *IEEE Trans. Control Syst. Technol.*, vol. 21, no. 5, pp. 1924-1930, Sep. 2013.
- [34] T. Lee, "Global Exponential Attitude Tracking Controls on SO(3)," *IEEE Trans. Autom. Control*, vol. 60, no. 10, pp. 2837-2842, Feb. 2015.
- [35] K. Lu and Y. Xia, "Adaptive attitude tracking control for rigid spacecraft with finite-time convergence," *Automatica*, vol. 49, no. 12, pp. 3591-3599, Dec. 2013.
- [36] D. Zhao and D. Yang, "Model-free control of quad-rotor vehicle via finite-time convergent extended state observer," *Inter. J. Cont. Auto. Sys.*, vol. 14, no. 1, pp. 242-254, Feb. 2016.
- [37] J. E. Bluman, C. K. Kang, and Y. Shtessel, "Control of a flapping-wing micro air vehicle: sliding-mode approach," *J. Guid. Control Dyn.*, vol. 41, no. 5, pp. 1223-1226, Apr. 2018.
- [38] J. A. Sanders, V. Ferdinand, and J. A. Murdock. *Averaging methods in nonlinear dynamical systems*, vol. 59, New York: Springer, 2007.